

CINDy: Conditional gradient-based Identification of Non-linear Dynamics – Noise-robust recovery

Alejandro Carderera

*School of Industrial and Systems Engineering, Georgia Institute of Technology, USA
Zuse Institute Berlin, Germany*

ALEJANDRO.CARDERERA@GATECH.EDU

Sebastian Pokutta

*Institute of Mathematics, Technische Universität Berlin, Germany
Zuse Institute Berlin, Germany*

POKUTTA@MATH.TU-BERLIN.DE

Christof Schütte

*Institute of Mathematics, Freie Universität Berlin, Germany
Zuse Institute Berlin, Germany*

SCHUETTE@MI.FU-BERLIN.DE

Martin Weiser

Zuse Institute Berlin, Germany

WEISER@ZIB.DE

Abstract

Governing equations are essential to the study of nonlinear dynamics, often enabling the prediction of previously unseen behaviors as well as the inclusion into control strategies. The discovery of governing equations from data thus has the potential to transform data-rich fields where well-established dynamical models remain unknown. This work contributes to the recent trend in data-driven sparse identification of nonlinear dynamics of finding the best sparse fit to observational data in a large library of potential nonlinear models. We propose an efficient first-order Conditional Gradient algorithm for solving the underlying optimization problem. In comparison to the most prominent alternative algorithms, the new algorithm shows significantly improved performance on several essential issues like sparsity-induction, structure-preservation, noise robustness, and sample efficiency. We demonstrate these advantages on several dynamics from the field of synchronization, particle dynamics, and enzyme chemistry.

1. Introduction

Many of the developments of physics have stemmed from our ability to describe natural phenomena in terms of differential equations. These equations have helped build our understanding of natural phenomena in fields as wide-ranging as classical mechanics, electromagnetism, fluid dynamics, neuroscience and quantum mechanics. They have also enabled key technological advances such as the combustion engine, the laser, or the transistor.

The modern age of Machine Learning and Big Data has heralded an age of *data-driven* models, in which the phenomena we explain are described in terms of statistical relationships and static data. Given sufficient data, we are able to train neural networks to classify, or to predict, with high accuracy, without the underlying model having any apparent knowledge of how the data was generated, or its structure. This makes the task of classifying, or predicting, on out-of-sample data a particularly challenging task. On the other hand, there has been a recent surge in interest in recovering the differential equations with which the data, often coming from a physical system, have been generated. This enables us to better understand how the data is generated, and to better predict on out-of-sample data, as opposed to using other learning approaches. Moreover, learning governing equations also permits understanding the mechanisms underlying the observed dynamical behavior; this is key to further scientific progress.

The seminal work of (Schmidt & Lipson, 2009) used symbolic regression to search the space of mathematical expressions, in order to find one that adequately fits the data. This entails randomly combining mathematical operations, analytical functions, state variables and constants and selecting those that show promise. These are later randomly expanded and combined in search of an expression that represents the data sufficiently well. Related to this approach is the *Approximate Vanishing Ideal* Algorithm (Heldt et al., 2009), based on the combination of Gröbner and Border bases with total least-squares regression, where a set of polynomials over (arbitrary) basis functions is successively expanded to capture all relations approximately satisfied by the data. A more recent algorithm, known as the *Sparse Identification of Nonlinear Dynamics* (SINDy) algorithm assumes that we have access to a library of predefined basis functions, and the problem becomes that of finding a linear combination of basis functions that best predicts the data at hand. This is done using sequentially-thresholded least-squares, in order to recover a sparse linear combination of basis functions (and potentially the coordinate system) that is able to represent the underlying phenomenon well (Brunton et al., 2016; Champion et al., 2019). This algorithm works extremely well when using noise-free data, but often produces dense solutions when the data is contaminated with noise. There have been several suggestions to deal with this, from more noise-robust non-convex problem formulations (Schaeffer & McCalla, 2017), to problem formulations that involve both learning the dynamic, and the noise contaminating the underlying data (Rudy et al., 2019; Kaheman et al., 2020). Neither of these approaches is computationally efficient for high-dimensional problems, the former having the additional drawback that the problem formulation is non-convex.

1.1 Contributions

In this paper we present a *Conditional gradient-based Identification of Non-linear Dynamics* algorithm, dubbed CINDy, in homage to the influential SINDy algorithm presented in (Brunton et al., 2016), a sparsity-inducing optimization algorithm that can be used to solve convex formulations of the sparse recovery problem. CINDy is a first-order convex optimization algorithm based on the *Conditional Gradient* (CG) algorithm (Levitin & Polyak, 1966) (also known as the Frank-Wolfe algorithm (Frank & Wolfe, 1956)) that brings together many of the advantages of existing sparse recovery techniques into a single algorithm. As documented in detail below, we compared CINDy to the most prominent alternative algorithms for solving the respective learning problem (SINDy, FISTA, IPM) with the following results:

1. **Sparsity-inducing.** The CG-based algorithm has an implicit bias for sparse solutions through the way it builds its iterates. Other existing approaches are forced to ensure sparsity through thresholding, or through problem formulations that encourage sparsity. This has a major impact on the *structural generalization behavior*, where CINDy significantly outperforms other methods leading to much more accurate trajectory predictions in the presence of noise.
2. **Structure-preserving dynamic.** The CINDy algorithm can easily incorporate underlying symmetries and conservation laws into the learning problem, resulting in learned dynamics consistent with the true physics, with minimal impact on the running time of the algorithm but significantly reducing sample complexity (due to reduced degrees of freedom) and improved generalization performance.
3. **Noise robustness.** When it comes to recovery of dynamics in the presence of noise, we will demonstrate a significant advantage of CINDy of about one to two orders of magnitude in recovery error *with respect to the true dynamic*, rather than just out-of-sample errors. This is largely due to the sparsity induced by the underlying CG method.
4. **Sample efficiency and large-scale learning.** Finally we will demonstrate that, given a certain noise level, CINDy will require significantly fewer samples to recover the dynamic with a given accuracy. Moreover, being a first-order method our approach naturally allows for the learning of large-scale dynamics, allowing even the use of stochastic first-order information in the extremely large-scale regime.
5. **Black-box implementation.** We provide an implementation of CINDy that can be used as a black-box not requiring any specialized knowledge in CG methods. The source code is made available under <https://github.com/ZIB-IOL>. We hope that this stimulates research in the use of CG-based algorithm for sparse recovery.

1.2 Preliminaries

We denote vectors using bold lower-case letters, and matrices using upper-case letters. We will use x_i to refer to the i -th element of the vector \mathbf{x} , and $X_{i,j}$ to refer to the element on the i -th row and j -th column of the matrix X . Let $\|\mathbf{x}\|$ and $\|\mathbf{x}\|_1$ denote the ℓ_2 and ℓ_1 norm of \mathbf{x} respectively, furthermore, let $\|\mathbf{x}\|_0$ denote the ℓ_0 norm¹, which is the number of non-zero elements in \mathbf{x} . Moreover, given a matrix $X \in \mathbb{R}^{n \times m}$ for $p, q \geq 1$ let $\|X\|_{p,q} = \left(\sum_{j=1}^m \left(\sum_{i=1}^n |X_{i,j}|^p \right)^{q/p} \right)^{1/q}$ denote the $\ell_{p,q}$ norm of X . We will use $\|X\|_F = \|X\|_{2,2}$ to refer to the familiar *Frobenius norm* of a matrix, and $\|X\|_0$ to refer to the number of non-zero elements in X . Given a matrix $X \in \mathbb{R}^{m \times n}$ let $\text{vec}(X) \in \mathbb{R}^{mn}$ denote the vectorization of the matrix X , that is the stacking $\text{vec}(X) = [X_{1,1}, \dots, X_{m,1}, \dots, X_{1,2}, \dots, X_{m,2}, \dots, X_{n,1}, \dots, X_{m,n}]^T$. Given a non-empty set $\mathcal{S} \subset \mathbb{R}^n$ we refer to its *convex hull* as $\text{conv}(\mathcal{S})$. The trace of the square matrix $X \in \mathbb{R}^{n \times n}$ will be denoted by $\text{trace}(X)$. We use $\dot{\mathbf{x}}(t)$ to denote the derivative of $\mathbf{x}(t)$ with respect to time, denoted by t , that is, $\dot{\mathbf{x}}(t) = \frac{d\mathbf{x}(t)}{dt}$. Given two integers $i \in \mathbb{Z}$ and $j \in \mathbb{Z}$ with $i \leq j$ we use $\llbracket i, j \rrbracket$ to denote the set $\{k \in \mathbb{Z} \mid i \leq k \leq j\}$. The vector with all entries equal to one is denoted by $\mathbf{1}_d \in \mathbb{R}^d$. Lastly, we use Δ_d to denote the unit probability simplex of dimension d , that is, the set $\Delta_d = \{\mathbf{x} \in \mathbb{R}^d \mid \mathbf{1}_d^T \mathbf{x} = 1, \mathbf{x} \geq 0\}$.

2. Learning sparse dynamics

Many physical systems can be described in terms of ordinary differential equations of the form $\dot{\mathbf{x}}(t) = F(\mathbf{x}(t))$, where $\mathbf{x}(t) \in \mathbb{R}^d$ denotes the state of the system at time t and $F: \mathbb{R}^d \rightarrow \mathbb{R}^d$ can usually be expressed as a linear combination of simpler *ansatz functions* $\psi_i: \mathbb{R}^d \rightarrow \mathbb{R}$ belonging to a dictionary $\mathcal{D} = \{\psi_i \mid i \in \llbracket 1, n \rrbracket\}$. This allows us to express the dynamic followed by the system as $\dot{\mathbf{x}}(t) = F(\mathbf{x}(t)) = \Xi^T \psi(\mathbf{x}(t))$ where $\Xi \in \mathbb{R}^{n \times d}$ is a – typically sparse – matrix $\Xi = [\xi_1, \dots, \xi_d]$ formed by column vectors $\xi_i \in \mathbb{R}^n$ for $i \in \llbracket 1, n \rrbracket$ and $\psi(\mathbf{x}(t)) = [\psi_1(\mathbf{x}(t)), \dots, \psi_n(\mathbf{x}(t))]^T \in \mathbb{R}^n$. We can therefore write:

$$\dot{\mathbf{x}}(t) = \begin{bmatrix} -\xi_1 & - \\ \vdots & \\ -\xi_d & - \end{bmatrix} \begin{bmatrix} \psi_1(\mathbf{x}(t)) \\ \vdots \\ \psi_n(\mathbf{x}(t)) \end{bmatrix}. \quad (2.1)$$

Alternatively, one could also consider that for any $t \geq t_1$ we can write $\mathbf{x}(t) = \mathbf{x}(t_1) + \int_{t_1}^t \dot{\mathbf{x}}(\tau) d\tau = \mathbf{x}(t_1) + \int_{t_1}^t \Xi^T \psi(\mathbf{x}(\tau)) d\tau = \mathbf{x}(t_1) + \Xi^T \int_{t_1}^t \psi(\mathbf{x}(\tau)) d\tau$. In matrix form this results in:

$$\mathbf{x}(t) - \mathbf{x}(t_1) = \begin{bmatrix} -\xi_1 & - \\ \vdots & \\ -\xi_d & - \end{bmatrix} \begin{bmatrix} \int_{t_1}^t \psi_1(\mathbf{x}(\tau)) d\tau \\ \vdots \\ \int_{t_1}^t \psi_n(\mathbf{x}(\tau)) d\tau \end{bmatrix}, \quad (2.2)$$

In the absence of noise, if we are given a series of data points from the physical system $\{\mathbf{x}(t_i), \dot{\mathbf{x}}(t_i)\}_{i=1}^m$, then we know that:

$$\begin{bmatrix} \dot{\mathbf{x}}(t_1) & \cdots & \dot{\mathbf{x}}(t_m) \\ | & & | \end{bmatrix} = \begin{bmatrix} -\xi_1 & - \\ \vdots & \\ -\xi_d & - \end{bmatrix} \begin{bmatrix} \psi(\mathbf{x}(t_1)) & \cdots & \psi(\mathbf{x}(t_m)) \\ | & & | \end{bmatrix}.$$

Or alternatively, viewing the dynamic from an integral perspective, we have that:

$$\begin{bmatrix} \mathbf{x}(t_2) - \mathbf{x}(t_1) & \cdots & \mathbf{x}(t_m) - \mathbf{x}(t_1) \\ | & & | \end{bmatrix} = \begin{bmatrix} -\xi_1 & - \\ \vdots & \\ -\xi_d & - \end{bmatrix} \begin{bmatrix} \int_{t_1}^{t_2} \psi_1(\mathbf{x}(\tau)) d\tau & \cdots & \int_{t_1}^{t_m} \psi_1(\mathbf{x}(\tau)) d\tau \\ \vdots & \ddots & \vdots \\ \int_{t_1}^{t_2} \psi_n(\mathbf{x}(\tau)) d\tau & \cdots & \int_{t_1}^{t_m} \psi_n(\mathbf{x}(\tau)) d\tau \end{bmatrix}.$$

1. Technically, the ℓ_0 norm is not a norm.

If we collect the data in matrices $\delta X = [\mathbf{x}(t_2) - \mathbf{x}(t_1), \dots, \mathbf{x}(t_m) - \mathbf{x}(t_1)] \in \mathbb{R}^{d \times m-1}$, $\dot{X} = [\dot{\mathbf{x}}(t_1), \dots, \dot{\mathbf{x}}(t_m)] \in \mathbb{R}^{d \times m}$, $\Psi(X) = [\psi(\mathbf{x}(t_1)), \dots, \psi(\mathbf{x}(t_m))] \in \mathbb{R}^{n \times m}$, and $\Gamma(X) \in \mathbb{R}^{n \times m-1}$ with $\Gamma(X)_{i,j} = \int_{t_1}^{t_{j+1}} \psi_i(\mathbf{x}(\tau)) d\tau$, we can view the dynamic from two perspectives:

Differential approach	Integral approach
$\dot{X} = \Xi^T \Psi(X)$	$\delta X = \Xi^T \Gamma(X)$

Consequently, when we try to recover the sparsest dynamic that fits this dynamic, we can attempt to solve one of two problems, which we present in tandem:

Differential approach	Integral approach
$\underset{\substack{\dot{X} = \Omega^T \Psi(X) \\ \Omega \in \mathbb{R}^{n \times d}}}{\text{argmin}} \ \Omega\ _0.$	$\underset{\substack{\delta X = \Omega^T \Gamma(X) \\ \Omega \in \mathbb{R}^{n \times d}}}{\text{argmin}} \ \Omega\ _0. \quad (2.3)$

Note that in the previous problem formulation we are implicitly assuming that we can compute $\Gamma(X)_{i,j}$, which is usually never the case. In practice we have to resort to approximating the integrals using quadrature over the given data, that is, for example $\Gamma(X)_{i,j} \approx \frac{1}{2} \sum_{k=1}^j (\psi_i(\mathbf{x}(t_k)) + \psi_i(\mathbf{x}(t_{k+1})))$. If we have access to \dot{X} and X , it will make sense to attack the problem from a differential perspective, but if we only have access to X , and we have to estimate \dot{X} from data, there are occasions where we can benefit from the integral approach, as we can potentially estimate $\Gamma(X)$ more accurately than \dot{X} ; this can be true in particular in the presence of noise. Henceforth, we use \dot{X} and $\Gamma(X)$ to denote the approximate matrices computed using numerical rules, as opposed to the exact differential and integral matrices. Unfortunately, the problems shown in Equations (2.3) are notoriously difficult NP-hard combinatorial problems, due to the presence of the ℓ_0 norm in the objective function of the minimization problem of both optimization problems (Juditsky & Nemirovski, 2020). Moreover, if the data points are contaminated by noise, leading to noisy matrices \dot{Y} , δY , $\Psi(Y)$ and $\Gamma(Y)$, depending on the expressive power of the basis functions ψ_i for $i \in \llbracket 1, n \rrbracket$, it may not even be possible (or undesirable) to satisfy $\dot{Y} = \Omega^T \Psi(Y)$ or $\delta Y = \Omega^T \Gamma(Y)$ for any $\Omega \in \mathbb{R}^{n \times d}$. Thus one can attempt to solve, for a suitably chosen $\varepsilon > 0$:

Differential approach	Integral approach
$\underset{\substack{\ \dot{Y} - \Omega^T \Psi(Y)\ _F \leq \varepsilon \\ \Omega \in \mathbb{R}^{n \times d}}}{\text{argmin}} \ \Omega\ _0.$	$\underset{\substack{\ \delta Y - \Omega^T \Gamma(Y)\ _F \leq \varepsilon \\ \Omega \in \mathbb{R}^{n \times d}}}{\text{argmin}} \ \Omega\ _0. \quad (2.4)$

The most popular sparse recovery algorithm, dubbed SINDy (Brunton et al., 2016), solves a component-wise relaxation of a problem very closely related to the differential problem shown in Equation (2.4) (Zhang & Schaeffer, 2019). Each step of the SINDy algorithm consists of a least-squares step and a thresholding step. The coefficients that have been thresholded are discarded in future iterations, making the least-squares problem progressively smaller. More specifically this process, when applied to one of the components of the problem, converges to (one of) the local minimizers of:

$$\underset{\xi_j \in \mathbb{R}^d}{\text{argmin}} \sum_{i=1}^m \left\| \dot{x}_j(t_i) - \xi_j^T \psi(\mathbf{x}(t_i)) \right\|_2^2 + \alpha \|\xi_j\|_0,$$

for a suitably chosen $\alpha \geq 0$ (Zhang & Schaeffer, 2019) and for $j \in \llbracket 1, d \rrbracket$. This methodology was later extended to partial differential equations by alternating between ridge-regression steps (as opposed to least-squares steps) and thresholding steps in (Rudy et al., 2017).

In another seminal paper Schaeffer & McCalla (2017) framed the sparse recovery problem from an integral perspective for the first time, using the Douglas-Rachford algorithm (Combettes & Pesquet, 2011) to solve

the non-convex integral problem in Equation (2.4). They showed experimentally that when the data is contaminated with noise and information about the derivatives has to be computed numerically, it can be advantageous to use the integral approach, as opposed to the differential approach, as the numerical integration is more robust to noise than numerical differentiation.

However, both problem formulations in Equation (2.4) remain non-convex, and so as is often done in optimization, we can attempt to *convexify* the problematic term in the optimization problem, namely substituting the ℓ_0 norm for the ℓ_1 norm. Note that the smallest value of $p \geq 0$ that results in the norm $\|\cdot\|_{p,p}$ being convex is $p = 1$. This leads us to a problem, known as *basis pursuit denoising* (BPD) (Chen et al., 1998), which can be written as:

BDP Differential approach	BDP Integral approach
$\operatorname{argmin}_{\Omega \in \mathbb{R}^{n \times d}} \ \Omega\ _{1,1} \quad \ \dot{Y} - \Omega^T \Psi(Y)\ _F^2 \leq \epsilon$	$\operatorname{argmin}_{\Omega \in \mathbb{R}^{n \times d}} \ \Omega\ _{1,1} \quad \ \delta Y - \Omega^T \Gamma(Y)\ _F^2 \leq \epsilon \quad (2.5)$

for appropriately chosen $\epsilon > 0$. The formulation shown in Equation (2.5) initially developed by the signal processing community, is intimately tied to the *Least Absolute Shrinkage and Selection Operator* (LASSO) regression formulation (Tibshirani, 1996), developed in the statistics community, which takes the form:

LASSO Differential approach	LASSO Integral approach
$\operatorname{argmin}_{\Omega \in \mathbb{R}^{n \times d}} \ \dot{Y} - \Omega^T \Psi(Y)\ _F^2 \quad \ \Omega\ _{1,1} \leq \alpha$	$\operatorname{argmin}_{\Omega \in \mathbb{R}^{n \times d}} \ \delta Y - \Omega^T \Gamma(Y)\ _F^2 \quad \ \Omega\ _{1,1} \leq \alpha \quad (2.6)$

In fact, the differential approach to the LASSO problem shown in Equation (2.6) was used in (Schaeffer, 2017) in conjunction with the Douglas-Rachford algorithm (Combettes & Pesquet, 2011) to solve the sparse recovery problem. A variation of the LASSO problem was also used to recover the governing equations in chemical reaction systems (Hoffmann et al., 2019) using a sequential quadratic optimization algorithm. The following proposition formalizes the relationship between the BDP and the LASSO problems.

Proposition 2.1. *Foucart & Rauhut (2017)*[Proposition 3.2]

1. If Ξ is the unique minimizer of the BDP problem shown in Equation (2.5) with $\epsilon > 0$, then there exists an $\alpha \geq 0$ such that Ξ is the unique minimizer of the LASSO problem shown in Equation (2.6).
2. If Ξ is a minimizer of the LASSO problem shown in Equation (2.6) with $\alpha > 0$, then there exists an $\epsilon \geq 0$ such that Ξ is a minimizer of the BDP problem shown in Equation (2.5).

Both problems shown in Equation (2.5) and (2.6) have a convex objective function and a convex feasible region, which allows us to use the powerful tools and guarantees of convex optimization. These two formulations can also be recast as an unconstrained optimization problem (via Lagrange dualization) in which the ℓ_1 norm has been added to the objective function (see Foucart & Rauhut (2017) and Borwein & Lewis (2010) for more details). Moreover, there is a significant body of theoretical literature, both from the statistics and the signal processing community, on the conditions for which we can successfully recover the support of Ξ (see e.g., Wainwright (2009)), the uniqueness of the LASSO solutions (see e.g., Tibshirani et al. (2013)), or the robust reconstruction of phenomena from incomplete data (see e.g., Candès et al. (2006)), to name but a few results.

Remark 2.2 (From learning ODE's to learning PDE's). Section 2 so far has only dealt with the case where the dynamic is expressed as a *ordinary differential equation* (ODE). This framework can also be extended to deal with the case of a dynamic expressed as a *partial differential equation* (PDE), by simply adding the necessary partial derivatives as ansatz functions to the regression problem (Rudy et al., 2017).

2.1 Incorporating structure

Conservation laws are a fundamental pillar of our understanding of physical systems. These conservation laws stem from differentiable symmetries that are present in nature (Noether, 1918). Imposing these symmetry constraints in our sparse regression problem can potentially lead to better generalization performance under noise, reduced sample complexity, and to learned dynamics that are consistent with the symmetries present in the real world. Our approach allows for arbitrary polyhedral constraints to be added, i.e., linear inequality and equality constraints; boundedness will be ensured automatically due to the ℓ_1 norm constraint. In particular, there are two large classes of structural constraints that can be easily encoded into our learning problem.

2.1.1 CONSERVATION PROPERTIES

From a differential perspective, we often observe in dynamical systems that certain relations hold between the elements of $\dot{\mathbf{x}}(t)$. Such is the case in chemical reaction dynamics, where if we denote the rate of change of the i -th species by $\dot{x}_i(t)$, we might observe relations of the form $a_j \dot{x}_j(t) + a_k \dot{x}_k(t) = 0$ due to mass conservation, which relate the j -th and k -th species being studied.

In the case where these relations are linear, we know that for some $\mathcal{J} \subseteq \llbracket 1, d \rrbracket$ and all $t \geq 0$ we can write:

$$\sum_{j \in \mathcal{J}} a_j \dot{x}_j(t) = c. \tag{2.7}$$

We can encode Equation (2.7) into our learning problem by using the fact that $\dot{x}_j(t) = \xi_j^T \psi(\mathbf{x}(t))$ and imposing that for all data points $i \in \llbracket 1, m \rrbracket$

$$\sum_{j \in \mathcal{J}} a_j \xi_j^T \psi(\mathbf{x}(t_i)) = c,$$

which can be expressed more succinctly as

$$\sum_{j \in \mathcal{J}} a_j \xi_j^T \Psi(X) = c \mathbf{1}_m.$$

This involves the addition of m linear constraints into our learning problem, which in the absence of noise does not pose any problems. However, when the data $\{\mathbf{x}(t_i), \dot{\mathbf{x}}(t_i)\}_{i=1}^m$ is contaminated by noise, and we only have access to $\{\mathbf{y}(t_i), \dot{\mathbf{y}}(t_i)\}_{i=1}^m$, it is futile to assume that $\sum_{j \in \mathcal{J}} a_j \dot{y}_j(t_i) = c$ for all $i \in \llbracket 1, m \rrbracket$ or that

$\sum_{j \in \mathcal{J}} a_j \xi_j^T \Psi(Y) = c \mathbf{1}_m$. In this case, it is more reasonable to assume that the derivatives are approximately preserved, and instead impose for some $\varepsilon > 0$ and all $i \in \llbracket 1, m \rrbracket$ that:

$$\left| \sum_{j \in \mathcal{J}} a_j \xi_j^T \psi(\mathbf{y}(t_i)) - c \right| \leq \varepsilon.$$

The addition of this constraint to the problem in Equation (2.6) preserves the convexity of the original problem. Moreover, the feasible region of the optimization problem remains polyhedral.

2.1.2 SYMMETRY BETWEEN VARIABLES

One of the key assumptions used in many-particle quantum systems is the fact the particles being studied are indistinguishable. And so it makes sense to assume that the effect that the i -th particle exerts on the j -th particle is the same as the effect that the j -th particle exerts on the i -th particle. The same can be said in classical mechanics for a collection of identical masses, where each mass is connected to all the other masses through identical springs. As an example, consider the system formed by two spring-coupled masses depicted in Figure 1.

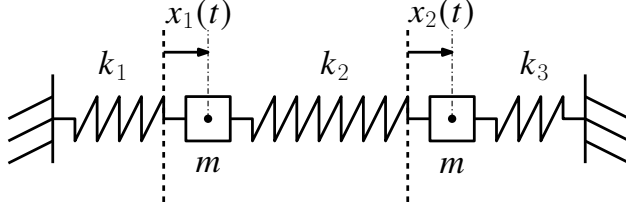


Figure 1: Two spring-coupled masses.

Here we denote the displacement of the center of mass of the i -th body from its equilibrium position at rest by $x_i(t)$. This allows us to express the dynamical evolution of the system by $m\ddot{x}_1(t) = -k_1x_1(t) + k_2(x_2(t) - x_1(t))$ and $m\ddot{x}_2(t) = -k_2(x_2(t) - x_1(t)) - k_3x_2(t)$. Suppose we are given access to a series of noisy data points $\{\ddot{\mathbf{y}}(t_i), \mathbf{y}(t_i)\}_{i=1}^m$ and we want to learn the dynamic $\ddot{\mathbf{y}}(t) = [\ddot{y}_1(t), \ddot{y}_2(t)]$ with a dictionary $\mathcal{D} = \{\psi_1(\mathbf{y}) = 1, \psi_2(\mathbf{y}) = y_1, \psi_3(\mathbf{y}) = y_2\}$ of basis functions of polynomials of degree up to one. The problem is analogous to that of learning $\dot{\mathbf{x}}(t)$ and can be framed similarly to that of Equation (2.6), substituting \dot{Y} for \ddot{Y} . If we use $\xi_j(\psi(\mathbf{x}))$ to refer to the coefficient in ξ_j , where ξ_j is the j -th column of Ω , associated with the basis function $\psi(\mathbf{x})$, we can write:

$$\hat{\Xi} = \underset{\substack{\|\Omega\|_{1,1} \leq \tau \\ \Omega \in \mathbb{R}^{n \times d}}}{\operatorname{argmin}} \left\| \begin{bmatrix} \ddot{y}_1(t_1) & \cdots & \ddot{y}_1(t_m) \\ \ddot{y}_2(t_1) & \cdots & \ddot{y}_2(t_m) \end{bmatrix} - \begin{bmatrix} \xi_1(1) & \xi_1(y_1) & \xi_1(y_2) \\ \xi_2(1) & \xi_2(y_1) & \xi_2(y_2) \end{bmatrix} \begin{bmatrix} 1 & \cdots & 1 \\ y_1(t_1) & \cdots & y_1(t_m) \\ y_2(t_1) & \cdots & y_2(t_m) \end{bmatrix} \right\|_F^2. \quad (2.8)$$

Where we have that $\xi_1 = [\xi_1(1), \xi_1(y_1), \xi_1(y_2)]$ and $\xi_2 = [\xi_2(1), \xi_2(y_1), \xi_2(y_2)]$. In light of the structure of the system and its symmetry, it makes sense to add to the learning problem the constraint $\xi_1(y_2) = \xi_2(y_1)$, that is, the effect of $y_1(t)$ on $\ddot{y}_2(t)$ is the same as the effect of $y_2(t)$ on $\ddot{y}_1(t)$. These constraints can also be readily applied in the integral formulation of the recovery problem.

Several optimization algorithms have been suggested to deal with the addition of such linear constraints, using either a variation of the *thresholded least-squares* algorithm used in SINDy (Loiseau & Brunton, 2018) or through the use of a *sparse relaxed regularized regression* (SR3) framework, where a regularization term controls the trade-off between conditioning of the problem and the fidelity to the original problem. This framework results in a formulation that can be solved by iteratively solving a least-squares problem followed by a proximal problem (Champion et al., 2020; Zheng et al., 2018). In this paper we present an optimization algorithm which can easily and directly deal with the addition of linear constraints, and enforce them exactly, i.e., without the aforementioned trade-off.

3. Frank-Wolfe algorithms

For simplicity, let us assume that we are dealing with the differential formulation of the LASSO problem shown in Equation (2.6), thus we would like to solve

$$\underset{\substack{\|\Omega\|_{1,1} \leq \alpha \\ \Omega \in \mathbb{R}^{n \times d}}}{\operatorname{argmin}} f(\Omega), \quad (3.1)$$

where $f(\Omega) = \|\dot{Y} - \Omega^T \Psi(Y)\|_F^2$. This can be done using first-order projection-based algorithms such as *gradient descent* or *accelerated gradient descent*. Using the former, the iterate at iteration $k + 1$ can be expressed, for a

suitably chosen step size $\gamma_k > 0$ as:

$$\Omega_{k+1} = \underset{\substack{\|\Omega\|_{1,1} \leq \tau \\ \Omega \in \mathbb{R}^{n \times d}}}{\operatorname{argmin}} \|\Omega - (\Omega_k - \gamma_k \nabla f(\Omega_k))\|_F^2 \quad (3.2)$$

$$= \underset{\substack{\|\Omega\|_{1,1} \leq \tau \\ \Omega \in \mathbb{R}^{n \times d}}}{\operatorname{argmin}} \left\| \Omega - \Omega_k - 2\gamma_k \Psi(Y) \left(\dot{Y} - \Omega_k^T \Psi(Y) \right)^T \right\|_F^2. \quad (3.3)$$

Fortunately, the quadratic problem shown in Equation (3.3) can be solved exactly with complexity $\mathcal{O}(nd)$ (Condat, 2016) (as this is equivalent to projecting a flattened version of the matrix onto the ℓ_1 polytope of dimension nd). If we were to add L additional linear constraints to the problem in Equation (2.6) to reflect the underlying structure of the dynamical system through symmetry and conservation, we would arrive at a polytope \mathcal{P} of the form

$$\mathcal{P} = \{ \Omega \in \mathbb{R}^{n \times d} \mid \|\Omega\|_{1,1} \leq \tau, \operatorname{trace}(A_l^T \Xi) \leq b_l, l \in \llbracket 1, L \rrbracket \},$$

with $A_l \in \mathbb{R}^{n \times d}$ and $b_l \in \mathbb{R}$ for all $l \in \llbracket 1, L \rrbracket$. So in this case, with additional structural constraints, the problem would transform into:

$$\underset{\substack{\Omega \in \mathcal{P} \\ \Omega \in \mathbb{R}^{n \times d}}}{\operatorname{argmin}} \|\dot{Y} - \Omega^T \Psi(Y)\|_F^2. \quad (3.4)$$

Unfortunately, in general there is no closed-form solution to the projection operator onto \mathcal{P} , and so in order to use projection-based algorithms to solve the optimization problem, one has to compute these projections approximately. Note that computing a projection onto \mathcal{P} is equivalent to solving a quadratic problem over \mathcal{P} , which can be as expensive as solving the original quadratic problem shown in Equation (3.4). In light of this difficulty, one can opt to solve the optimization problem using projection-free algorithms like the *Frank-Wolfe* (FW) algorithm (Frank & Wolfe, 1956) (also known as the *Conditional Gradients* algorithm (Levitin & Polyak, 1966), shown in Algorithm 1 with exact line search).

Algorithm 1: CG algorithm applied to (3.4)

Input : Initial point $\Omega_1 \in \mathcal{P}$.

Output : Point $\Omega_{K+1} \in \mathcal{P}$.

```

1 for  $k = 1$  to  $K$  do
2    $\nabla f(\Omega_k) \leftarrow 2\Psi(Y) (\dot{Y} - \Omega_k^T \Psi(Y))^T$ 
3    $V_k \leftarrow \underset{\Omega \in \mathcal{P}}{\operatorname{argmin}} \operatorname{trace}(\Omega^T \nabla f(\Omega_k))$ 
4    $D_k \leftarrow V_k - \Omega_k$ 
5    $\gamma_k \leftarrow \min \left\{ -\frac{1}{2} \frac{\operatorname{trace}(D_k^T \nabla f(\Omega_k))}{\|D_k^T \Psi(Y)\|_F^2}, 1 \right\}$ 
6    $\Omega_{k+1} \leftarrow \Omega_k + \gamma_k D_k$ 
7 end
```

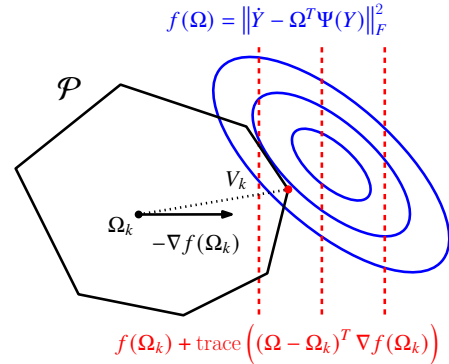


Figure 2: CG algorithm schematic.

This family of algorithms (including Algorithm 1) requires solving a linear optimization problem over a polytope (Line 3 of Algorithm 1) at each iteration, instead of a quadratic problem. As the iterates are obtained as a convex combination of the current iterate Ω_k and the solution of the linear optimization problem over \mathcal{P} , denoted by V_k (Line 3 of Algorithm 1), thus always ensuring feasibility, these methods are *projection-free*. The direction $V_k - \Omega_k$ is the direction that best approximates (in the inner product sense) the negative of the gradient of the objective function at the current iterate Ω_k , in this case $-\nabla f(\Omega_k) = -2\Psi(Y) (\dot{Y} - \Omega_k^T \Psi(Y))^T$,

if we restrict ourselves to moving towards vertices of the polytope \mathcal{P} . To be more precise:

$$\begin{aligned} \text{trace} \left(- (V_k - \Omega_k)^T \nabla f(\Omega_k) \right) &= \max_{\Omega \in \mathcal{P}} \text{trace} \left(- (\Omega - \Omega_k)^T \nabla f(\Omega_k) \right) \\ &= \max_{\Omega \in \mathcal{P}} \text{trace} \left(-2 (\Omega - \Omega_k)^T \Psi(Y) \left(\dot{Y} - \Omega_k^T \Psi(Y) \right)^T \right). \end{aligned}$$

This can be seen as equivalent to moving along the direction given by the vertex which minimizes a linear approximation of the objective function at the current iterate Ω_k over the polytope \mathcal{P} (see Figure 2, where we have denoted the objective function as $f(\Omega) = \|\dot{Y} - \Omega^T \Psi(Y)\|_F^2$), that is:

$$\begin{aligned} V_k &= \underset{\Omega \in \mathcal{P}}{\text{argmin}} f(\Omega_k) + \text{trace} \left((\Omega - \Omega_k)^T \nabla f(\Omega_k) \right) \\ &= \underset{\Omega \in \mathcal{P}}{\text{argmin}} \|\dot{Y} - \Omega_k^T \Psi(Y)\|_F^2 + 2 \text{trace} \left((\Omega - \Omega_k)^T \Psi(Y) \left(\dot{Y} - \Omega_k^T \Psi(Y) \right)^T \right). \end{aligned}$$

Once the vertex V_k has been found, the exact line search solution is computed in Line 5 to find the step size γ_k that results in the greatest decrease in primal gap, that is, $\gamma_k = \underset{\gamma \in [0,1]}{\text{argmin}} f(\Omega_k + \gamma(V_k - \Omega_k))$. Fortunately, as the function being minimized (see Equation (3.4)) is a quadratic, there is a closed form expression for the optimal step size. Note that the step size in Line 5 is always non-negative and the clipping ensures that we build convex combinations; the clipping is active (if at all) only in the very first iteration by standard arguments (see, e.g., (Braun et al., 2021)).

Remark 3.1. If we assume that the starting point Ω_1 is a vertex of the polytope, then we know that the iterate Ω_k can be expressed as a convex combination of at most k vertices of \mathcal{P} . This is due to the fact that the algorithm can pick up no more than one vertex per iteration. Note that the CG algorithm applied to the problem shown in Equation (3.1), where the feasible region is the ℓ_1 ball without any additional constraints, picks up at most one basis function in the k -th iteration, as $V_k^T \psi(\mathbf{x}(t)) = \pm \tau \psi_i(\mathbf{x}(t))$ for some $i \in \llbracket 1, n \rrbracket$. This means that if we use the Frank-Wolfe algorithm to solve a problem over the ℓ_1 ball, we encourage sparsity not only through the regularization provided by the ℓ_1 ball, but also *through the specific nature of the Frank-Wolfe algorithm* independently of the size of the feasible region. In practice, when using, e.g., early termination due to some stopping criterion, this results in the Frank-Wolfe algorithm producing sparser solutions than projection-based algorithms (such as projected gradient descent, which typically use dense updates) when applied to Problem 3.4, despite the fact that both algorithms converge to the same solution if the problem is strictly convex.

Thus, in addition to the trade-off between reconstruction accuracy and sparsity offered by LASSO formulations parametrized by the size α of the ℓ_1 ball, we have the same trade-off in terms of the iteration count. Similar to iterative or semi-iterative regularization methods such as Landweber’s method for ill-posed linear problems in Hilbert spaces (Hanke, 1991), reconstruction accuracy improves in iterations, while the norm of the solution, in our case the l_0 norm, tends to grow. The trade-off can be decided by a termination criterion, e.g., a sufficiently small residual in Morozow’s discrepancy principle (Morozov, 1966) or, in our case, a sufficiently small primal gap.

One of the interesting properties of Conditional Gradient algorithms is the fact that, since f is convex, at each iteration we can compute the *Frank-Wolfe* gap, an upper bound on the primal gap, at no extra cost.

Definition 3.2 (Frank-Wolfe gap). The Frank-Wolfe gap of the function f over the feasible region \mathcal{P} evaluated at Ω_k , denoted by $g_{\mathcal{P}}(\Omega)$, is given by:

$$g_{\mathcal{P}}(\Omega_k) = \max_{\Omega \in \mathcal{P}} \text{trace} \left((\Omega_k - \Omega)^T \nabla f(\Omega_k) \right).$$

To see why this quantity provides an upper bound on the primal gap $f(\Omega_k) - \min_{\Omega \in \mathcal{P}} f(\Omega)$, when $f(\Omega)$ is convex, note that if we denote $\Omega^* = \operatorname{argmin}_{\Omega \in \mathcal{P}} f(\Omega)$, then

$$f(\Omega_k) - f(\Omega^*) \leq \operatorname{trace} \left((\Omega_k - \Omega^*)^T \nabla f(\Omega_k) \right) \quad (3.5)$$

$$\leq \max_{\Omega \in \mathcal{P}} \operatorname{trace} \left((\Omega_k - \Omega)^T \nabla f(\Omega_k) \right) \quad (3.6)$$

$$= \operatorname{trace} \left((\Omega_k - V_k)^T \nabla f(\Omega_k) \right), \quad (3.7)$$

holds with Equation (3.5) following from convexity of f .

To sum up the advantages of CG algorithms when applied to structured sparse LASSO recovery problems:

1. Sparsity is encouraged through a two-fold approach: through the ℓ_1 regularization used in the problem formulation and through the use of the Conditional Gradient algorithms, which are sparse in nature.
2. Linear equality and inequality constraints can be added easily and naturally to the constraint set of the problem to reflect symmetry or conservation assumptions. These additional constraints can be efficiently managed due to the fact that there are extremely efficient algorithms to solve linear programs over polytopes.

These characteristics make the class of Conditional Gradient methods extremely attractive versus projection-based algorithms to solve LASSO recovery problems.

3.1 Fully-Corrective Conditional Gradients

For the recovery of sparse dynamics from data, one of the most interesting algorithms in terms of sparsity is the *Fully-Corrective Conditional Gradient* (FCCG) algorithm (Algorithm 2). This algorithm picks up a vertex V_k from the polytope \mathcal{P} at each iteration (Line 4 of Algorithm 2) and reoptimizes over the convex hull of $\mathcal{S}_k \cup V_k$ (Line 6 of Algorithm 2), which is the union of the vertices picked up in previous iterations, and the new vertex V_k . The reoptimization step can potentially remove a large number of unnecessary vertices picked up in earlier iterations.

Algorithm 2: Fully-Corrective Conditional Gradient (CG) algorithm applied to Problem (3.4)

Input : Initial point $\Omega_1 \in \mathcal{P}$.

Output : Point $\Omega_{K+1} \in \mathcal{P}$.

```

1  $\mathcal{S}_1 \leftarrow \emptyset$ 
2 for  $k = 1$  to  $K$  do
3    $\nabla f(\Omega_k) \leftarrow 2\Psi(Y) (\dot{Y} - \Omega_k^T \Psi(Y))^T$ 
4    $V_k \leftarrow \operatorname{argmin}_{\Omega \in \mathcal{P}} \operatorname{trace}(\Omega^T \nabla f(\Omega_k))$ 
5    $\mathcal{S}_{k+1} \leftarrow \mathcal{S}_k \cup V_k$ 
6    $\Omega_{k+1} \leftarrow \operatorname{argmin}_{\Omega \in \operatorname{conv}(\mathcal{S}_{k+1})} \|\dot{Y} - \Omega^T \Psi(Y)\|_F^2$ 
7 end
```

The reoptimization subproblem shown in Line 6 of Algorithm 2 is a quadratic problem over a polytope \mathcal{P} , like the original problem in Equation (3.4). However, it can be rewritten as an optimization problem over the unit probability simplex of dimension k , as the cardinality of the set \mathcal{S}_{k+1} satisfies $|\mathcal{S}_{k+1}| = k$. To see this, note that given a set $\mathcal{S}_{k+1} \subseteq \operatorname{vert}(\mathcal{P})$ we can express any $\Omega \in \operatorname{conv}(\mathcal{S}_{k+1})$ as $\Omega = \sum_{i=1}^k \lambda_i V_i$ for some

$\lambda = [\lambda_1, \dots, \lambda_k] \in \Delta_k$ and $V_i \in \mathcal{S}_{k+1}$ for all $i \in \llbracket 1, k \rrbracket$. This leads to:

$$\begin{aligned} \min_{\Omega \in \text{conv}(\mathcal{S}_{k+1})} \|\dot{Y} - \Omega^T \Psi(Y)\|_F^2 &= \min_{\Omega \in \text{conv}(\mathcal{S}_{k+1})} \left(\text{trace}(\dot{Y}^T \dot{Y}) - 2 \text{trace}(\Omega^T \Psi(Y) \dot{Y}^T) + \text{trace}(\Omega^T \Psi(Y) \Psi(Y)^T \Omega) \right) \\ &= \min_{\lambda \in \Delta^k} \left(\|\dot{Y}\|_F^2 - 2 \sum_{i=1}^k \lambda_i \text{trace}(V_i^T \Psi(Y) \dot{Y}^T) + \sum_{i=1}^k \sum_{j=1}^k \lambda_i \lambda_j \text{trace}(V_i^T \Psi(Y) \Psi(Y)^T V_j) \right). \end{aligned}$$

Which can be expressed more succinctly if we denote $\Lambda_{k+1} = [\text{vec}(V_1^T \Psi(Y)), \dots, \text{vec}(V_k^T \Psi(Y))] \in \mathbb{R}^{dm \times k}$ and we write:

$$\min_{\Omega \in \text{conv}(\mathcal{S}_{k+1})} \|\dot{Y} - \Omega^T \Psi(Y)\|_F^2 = \min_{\lambda \in \Delta^k} \left(\|\dot{Y}\|_F^2 - 2 \text{vec}(\dot{Y})^T \Lambda_{k+1} \lambda + \lambda^T \Lambda_{k+1}^T \Lambda_{k+1} \lambda \right) \quad (3.8)$$

$$= \min_{\lambda \in \Delta^k} \|\Lambda_{k+1} \lambda - \text{vec}(\dot{Y})\|^2. \quad (3.9)$$

So in order to solve the optimization problem in Line 6 of Algorithm 2 we would need to solve the optimization problem shown in Equation (3.9) (which is also convex, as convexity is invariant under affine maps) and take $\Omega = \sum_{i=1}^k \lambda_i V_i$. While the original quadratic problem over \mathcal{P} , shown in Equation (3.4), has dimensionality $n \times d$, the quadratic problem shown in Line 6 of Algorithm 2 has dimensionality k when it is solved in λ -space, which leads to improved convergence due to reduced problem dimensionality.

Remark 3.3. If the polytope \mathcal{P} being considered is simply the ℓ_1 ball, then computing Λ_{k+1} requires at most mk multiplications, since in this case $\|V_i\|_0 = 1$ for all $i \in \llbracket 1, k \rrbracket$, as V_i is simply one of the vertices of the ℓ_1 ball (which is a polytope), and so computing $\text{vec}(V_i^T \Psi(Y))$ requires at most m multiplications for each i . This means that Λ_{k+1} is sparse, as $\|\Lambda_{k+1}\|_0 \leq mk$, which allows us to efficiently compute $\Lambda_{k+1}^T \Lambda_{k+1} \in \mathbb{R}^{k \times k}$ and $\text{vec}(\dot{Y})^T \Lambda_{k+1} \in \mathbb{R}^k$.

Remark 3.4. If additional constraints are added to the ℓ_1 ball, in general, we cannot make any statements about the sparsity of Λ_{k+1} , other than in numerical experiments we observe that $\|\Lambda\|_0 \ll dm k$.

Due to the fact that there are efficient algorithms to compute projections onto the probability simplex of dimension k with complexity $\mathcal{O}(k)$ (Condat, 2016) we can use accelerated projected gradient descent to solve the subproblems in Line 6 of Algorithm 2 (Nesterov, 1983; 2018) (shown in Algorithm 4 and Algorithm 5 in Appendix B). Solving the problem shown in Line 6 of Algorithm 2 to optimality at each iteration is computationally prohibitive, and so ideally we would like to solve the problem in Line 6 to ε_k -optimality.

3.2 Blended Conditional Gradients

This leads to the question: How should we choose ε_k at each iteration k , if we want to find an ε -optimal solution to the problem shown in Equation (3.4)? Computing a solution to the problem shown in Line 6 to accuracy $\varepsilon_k = \varepsilon$ at each iteration might be way too computationally expensive. Conceptually, we need relatively inaccurate solutions for early iterations where $\Omega^* \notin \text{conv}(\mathcal{S}_{k+1})$, requiring only accurate solutions when $\Omega^* \in \text{conv}(\mathcal{S}_{k+1})$. At the same time we do not know whether we have found \mathcal{S}_{k+1} so that $\Omega^* \in \text{conv}(\mathcal{S}_{k+1})$.

The rationale behind the *Blended Conditional Gradient* (BCG) algorithm (Braun et al., 2019) (the variant used for our specific problem is shown in Algorithm 3) is to provide an explicit value of the accuracy ε_k needed at each iteration starting with rather large ε_k in early iterations and progressively getting more accurate when approaching the optimal solution; the process is controlled by an optimality gap measure. In some sense one might think of BCG as a practical version of FCCG with stronger convergence guarantees and much faster real-world performance.

The algorithm *approximately* minimizes $f(\Omega)$ over $\text{conv}(\mathcal{S}_k)$ in Line 5 of Algorithm 3. This problem is analogous to the one shown in Equation (3.9) and can be solved in the space of λ barycentric coordinates. The approximate minimization is carried out until the Frank-Wolfe gap satisfies $g_{\text{conv}(\mathcal{S}_k)}(\Omega_{k+1}) \leq \Phi$. The algorithm then computes the Frank-Wolfe gap over \mathcal{P} in Lines 7-8, that is $g_{\mathcal{P}}(\Omega_{k+1})$. If this is smaller than the accuracy Φ to which we are computing the solutions in Line 5, we increase the accuracy to which we

Algorithm 3: CINDy: Blended Conditional Gradient (BCG) algorithm variant applied to Problem (3.4)

Input : Initial point $\Omega_0 \in \mathcal{P}$.

Output : Point $\Omega_{K+1} \in \mathcal{P}$.

```

1  $\Omega_1 \leftarrow \operatorname{argmin}_{\Omega \in \mathcal{P}} \operatorname{trace}(\Omega^T \nabla f(\Omega_0))$ 
2  $\Phi \leftarrow \operatorname{trace}\left((\Omega_0 - \Omega_1)^T \nabla f(\Omega_0)\right) / 2$ 
3  $\mathcal{S}_1 \leftarrow \{\Omega_1\}$ 
4 for  $k = 1$  to  $K$  do
5     Find  $\Omega_{k+1}$  such that  $g_{\operatorname{conv}(\mathcal{S}_k)}(\Omega_{k+1}) \leq \Phi$  ▷ Solve problem approximately
6      $\nabla f(\Omega_{k+1}) \leftarrow 2\Psi(Y)(\dot{Y} - \Omega_{k+1}^T \Psi(Y))^T$ 
7      $V_{k+1} \leftarrow \operatorname{argmin}_{\Omega \in \mathcal{P}} \operatorname{trace}(\Omega^T \nabla f(\Omega_{k+1}))$ 
8      $g_{\mathcal{P}}(\Omega_{k+1}) \leftarrow \operatorname{trace}\left((\Omega_{k+1} - V_{k+1})^T \nabla f(\Omega_{k+1})\right)$ 
9     if  $g_{\mathcal{P}}(\Omega_{k+1}) \leq \Phi$  then
10          $\Phi \leftarrow g_{\mathcal{P}}(\Omega_{k+1}) / 2$  ▷ Update accuracy
11          $\mathcal{S}_{k+1} \leftarrow \mathcal{S}_k$ 
12          $\Omega_{k+1} \leftarrow \Omega_k$ 
13     else
14          $\mathcal{S}_{k+1} \leftarrow \mathcal{S}_k \cup V_{k+1}$  ▷ Expand active set
15          $D_k \leftarrow V_{k+1} - \Omega_k$ 
16          $\gamma_k \leftarrow \min\left\{-\frac{1}{2} \operatorname{trace}(D_k^T \nabla f(\Omega_k)) / \|D_k^T \Psi(Y)\|_F^2, 1\right\}$ 
17          $\Omega_{k+1} \leftarrow \Omega_k + \gamma_k D_k$ 
18     end
19 end

```

compute the solutions in Line 10 by taking $\Phi = g_{\mathcal{P}}(\Omega_{k+1}) / 2$. This means that as we get closer to the solution of the optimization problem, and the gap $g_{\mathcal{P}}(\Omega_{k+1})$ decreases, we increase the accuracy to which we solve the problems over $\operatorname{conv}(\mathcal{S}_k)$. If on the other hand $g_{\mathcal{P}}(\Omega_{k+1})$ is larger than Φ , expanding the active set promised more progress than continuing optimizing over $\operatorname{conv}(\mathcal{S}_k)$. Thus, we potentially expand the active set in Line 14, and we perform a standard CG step with exact line search in Lines 15-17. Regarding the step size in Line 5 the same comments apply as in Section 3: it is always non-negative, ensures convex combinations, and the clipping, if active, is active only in the very first iteration.

The BCG algorithm enjoys robust theoretical convergence guarantees, and exhibits very fast convergence in practice. Moreover, it generally produces solutions with a high level of sparsity in the experiments essentially identical to those produced by FCCG. This makes the BCG algorithm a powerful alternative to the sequentially-thresholded least-squares approach followed in the SINDy algorithm (Brunton et al., 2016) (or the sequentially-thresholded ridge regression in Rudy et al. (2017)).

4. Numerical experiments

We benchmark the CINDy algorithm (Algorithm 3) applied to the LASSO formulations presented in Equation (2.6) with the following algorithms. Our main benchmark here is the SINDy algorithm, however we included two more popular optimization methods for further comparison.

SINDy: We use a SINDy algorithm implementation based on the Python implementation in the [PDE-FIND](#) Github repository from (Rudy et al., 2017) (which originally used ridge-regression, as opposed to the least-squares regression used in (Brunton et al., 2016)).

FISTA: The *Fast Iterative Shrinkage-Thresholding Algorithm* (Beck & Teboulle, 2009), commonly known as FISTA, is a first-order accelerated method commonly used to solve LASSO problems which are equivalent to the ones shown in Equation (2.6) (in which the ℓ_1 norm appears as a regularization term in the objective function, as opposed to a constraint).

IPM: *Interior-Point Methods* (IPM) are an extremely powerful class of convex optimization algorithms, able to reach a highly-accurate solution in a small number of iterations. The algorithms rely on the resolution of a linear system of equations at each iteration, which can be done efficiently if the underlying system is sparse. Unfortunately this is not the case for our LASSO formulations, which makes this algorithm impractical for large problems. We will use the path-following primal form interior-point method for quadratic problems described in (Andersen et al., 2011), and implemented in Python’s `CVXOPT`, to solve the LASSO problem in Equation (2.6) (with and without additional constraints, as described in Section 2.1).

We use CINDy (c) and CINDy to refer to the results achieved by the CINDy algorithm with and without the additional constraints described in Section 2.1. Likewise, we use IPM (c) and IPM to refer to the results achieved by the IPM algorithm with and without additional constraints. We have not added structural constraints to the formulation in the SINDy algorithm, as there is no straightforward way to include constraints in the original implementation, or the FISTA algorithm, as we would need to compute non-trivial proximal/projection operators, making the algorithm computationally expensive.

Remark 4.1 (Hyperparameter selection for the CINDy algorithm). In the experiments we have not tuned the ℓ_1 parameter in the LASSO formulation for the CINDy algorithm (neither in the integral nor the differential formulation), simply relying on $\alpha = 2 \|\dot{Y}\Psi(Y)^\dagger\|_{1,1}$ and $\alpha = 2 \|\delta Y \Gamma(Y)^\dagger\|_{1,1}$ in the differential and integral formulation for all the experiments. With this choice, purposefully, all computed solutions are located in the interior of the feasible region. It is important to note that due to this choice, *sparsity in the recovered dynamics is therefore due to implicit regularization by the CINDy optimization algorithm* and not due to binding constraints of the LASSO problem formulation.

Remark 4.2 (Hyperparameter selection for SINDy, FISTA and the IPM algorithm). We have selected the threshold coefficient for SINDy, and the ℓ_1 regularization parameters of FISTA and the IPM algorithm based on performance on testing data. In the differential and integral formulations we have selected the hyperparameters that gave the smallest value of $\|\dot{Y}_{\text{validation}} - \Omega^T \Psi(Y_{\text{validation}})\|_F^2$ and $\|\delta Y_{\text{validation}} - \Omega^T \Gamma(Y_{\text{validation}})\|_F^2$ respectively. Other criteria could be chosen to increase the level of sparsity of the solution, at the expense of accuracy in inferring derivatives/trajectories. Note that in the BCG algorithm, the sparsity-accuracy compromise is instead parametrized in terms of the stopping criterion instead of thresholds or ℓ_1 bounds. We hasten to stress however, that the sparsity of CINDy (and more precisely of the BCG algorithm) is due to *extremely sparse updates* in each iteration, whereas the other algorithms’ updates are *dense* and sparsity is only realized by means of postprocessing these updates or solutions.

Remark 4.3 (Stopping criterion). We use 200 rounds of thresholding and least-squares for each run of the SINDy algorithm (or until no more coefficients are thresholded in a given iteration). The threshold value that yields the best accuracy in terms of testing data is outputted afterwards. During the selection of the FISTA hyperparameter, the algorithm is run for a sufficiently large number of iterations until the primal progress made is below a tolerance of 10^{-8} . The same is done when we run the FISTA algorithm with the final hyperparameter selected. The IPM algorithm is run with the default stopping criterion parameters. Lastly, the CINDy algorithm is run until the Frank-Wolfe gap, an upper bound on the primal gap, is below a tolerance of 10^{-6} .

For each physical model in this section we generate a set of T points, simulating the physical model c different times, to generate c experiments. First, a random starting point for the j -th experiment is generated. This random starting point is used to generate a set of T/c points equally-spaced in time $\mathbf{x}^j(t_i)$ with $i \in \llbracket 1, T/c \rrbracket$ using a high-order Runge-Kutta scheme and ensuring that the discretization error $\|\mathbf{x}^j(t_i) - \mathbf{x}(t_i)\|$ is below a tolerance of 10^{-13} . The samples are then contaminated with i.i.d. Gaussian noise. If we denote the noisy data point at time t_i for the j -th experiment by $\mathbf{y}^j(t_i)$, we have

$$\mathbf{y}^j(t_i) = \mathbf{x}^j(t_i) + \eta \mathcal{N}(0, \Sigma),$$

where $\mathcal{N}(0, \Sigma)$ denotes the d -dimensional multivariate Gaussian distribution centered at zero with covariance matrix Σ , where

$$\Sigma = \text{diag} \left(\frac{1}{T} \sum_{i=1}^{T/c} \sum_{j=1}^c (x_1^j(t_i) - \mu_1)^2, \dots, \frac{1}{T} \sum_{i=1}^{T/c} \sum_{j=1}^c (x_d^j(t_i) - \mu_d)^2 \right) \quad (4.1)$$

$$\mu_k = \frac{1}{T} \sum_{i=1}^{T/c} \sum_{j=1}^c x_k^j(t_i). \quad (4.2)$$

We denote the noise level that we vary in our experiments by η . Note that the k -th element on the diagonal of Σ is simply the sample variance of the k -th component of points generated in the experiments.

Both $\Gamma(Y)$ and $\Psi(Y)$ are normalized so that their rows have unit variance, to make the learning process easier for all the algorithms. For the training of the algorithm, 70% of the data points are used, while 20% are used for validation and selecting the combination that gives the best hyperparameters (the ℓ_1 radius in the FISTA and IPM algorithms, or the threshold in SINDy's sequential thresholded least-squares algorithm). Lastly, the 10% remaining data points are used for evaluating the output of each algorithm, and are referred to as the testing set.

We would like to stress that, while it might seem that we are in the overdetermined regime in terms of the number of samples used in training, this is not accurate as due to the evolutionary nature, i.e., evolving the dynamic in time, for each of the experiments the samples obtained *within* one experiment are highly correlated.

The approximate derivatives are computed from noisy data using either local polynomial interpolation (Knowles & Renka, 2014). The matrix $\Gamma(Y)$ used in the integral formulation of the sparse recovery problem was computed through the integration of local polynomial interpolations. The same matrices and training-validation-testing split is used in each experiment for all the algorithms, to make a fair comparison. Section C in the Appendix shows the difference in accuracy that can be achieved with the different methods when estimating the derivatives and integrals for one physical model. Given the disparity in accuracy that can be achieved between the estimation of derivatives and integrals, we have decided to present the results for the integral and differential formulation separately.

4.1 Benchmark metrics

We benchmark the algorithms in terms of the following metrics, in a similar spirit as was done in (Kaheman et al., 2020). Given a dictionary of basis functions \mathcal{D} of cardinality n , an associated exact dynamic $\Xi \in \mathbb{R}^{n \times d}$ such that $\dot{\mathbf{x}}(t) = \Xi^T \psi(\mathbf{x}(t))$, and a dynamic $\Omega \in \mathbb{R}^{n \times d}$ outputted by the algorithms, we define:

Definition 4.4 (Recovery error). The *recovery error* \mathcal{E}_R of the algorithm is given by:

$$\mathcal{E}_R \stackrel{\text{def}}{=} \|\Omega - \Xi\|_F.$$

Given noisy data points $Y_{\text{testing}}, \dot{Y}_{\text{testing}}$ from the testing set we define:

Definition 4.5 (Derivative inference error). The *derivative inference error* \mathcal{E}_D of the algorithm is given by:

$$\mathcal{E}_D \stackrel{\text{def}}{=} \left\| (\Omega - \Xi)^T \Psi(Y_{\text{testing}}) \right\|_F.$$

This measure aims at quantifying how well the learned dynamics will infer the true derivatives at Y .

Definition 4.6 (Trajectory inference error). The *trajectory inference error* \mathcal{E}_T of the algorithm is given by:

$$\mathcal{E}_T \stackrel{\text{def}}{=} \left\| (\Omega - \Xi)^T \Gamma(Y_{\text{testing}}) \right\|_F.$$

This measure aims at quantifying how well the learned dynamics will infer the trajectory using the approximate matrix $\Gamma(Y)$, compared to the true dynamic Ξ .

In order to gauge how well a given algorithm is able to recover the true support of a dynamic, we define:

Definition 4.7 (Extraneous terms). The *extraneous terms* of a given dynamic $\Omega \in \mathbb{R}^{d \times n}$ with respect to its true counterpart $\Xi \in \mathbb{R}^{d \times n}$ is defined as:

$$\mathcal{S}_E \stackrel{\text{def}}{=} \left| \left\{ \Omega_{i,j} \mid \Omega_{i,j} \neq 0, \Xi_{i,j} = 0, i \in \llbracket 1, d \rrbracket, j \in \llbracket 1, n \rrbracket \right\} \right|.$$

This metric simply counts the terms picked up in Ω that are not present in the true physical model, represented by Ξ , i.e. it counts the false positives.

Definition 4.8 (Missing terms). The *missing terms* of a given dynamic $\Omega \in \mathbb{R}^{d \times n}$ with respect to its true counterpart $\Xi \in \mathbb{R}^{d \times n}$ is defined as:

$$\mathcal{S}_M \stackrel{\text{def}}{=} \left| \left\{ \Omega_{i,j} \mid \Omega_{i,j} = 0, \Xi_{i,j} \neq 0, i \in \llbracket 1, d \rrbracket, j \in \llbracket 1, n \rrbracket \right\} \right|.$$

This metric simply counts the terms that have not been picked up in Ω that actually participate in governing the true physical model, represented by Ξ , i.e. it counts the false negatives.

4.2 Kuramoto model

The Kuramoto model describes a large collection of d weakly coupled identical oscillators, that differ in their natural frequency ω_i (Kuramoto, 1975) (see Figure 3). This dynamic is often used to describe synchronization phenomena in physics, and has been previously used in the numerical experiments of a tensor-based algorithm for the recovery of large dynamics (Gelß et al., 2019). If we denote by x_i the angular displacement of the i -th oscillator, then the governing equation with external forcing (see (Acebrón et al., 2005)) can be written as:

$$\begin{aligned} \dot{x}_i &= \omega_i + \frac{K}{d} \sum_{j=1}^d \sin(x_j - x_i) + h \sin(x_i) \\ &= \omega_i + \frac{K}{d} \sum_{j=1}^d \left[\sin(x_j) \cos(x_i) - \cos(x_j) \sin(x_i) \right] + h \sin(x_i), \end{aligned}$$

for $i \in \llbracket 1, d \rrbracket$, where d is the number of oscillators (the dimensionality of the problem), K is the coupling strength between the oscillators and h is the external forcing parameter. The exact dynamic Ξ can be expressed using a dictionary of basis functions formed by sine and cosine functions of x_i for $i \in \llbracket 1, d \rrbracket$, and pairwise combinations of these functions, plus a constant term. To be more precise, the dictionary used is

$$\mathcal{D} = \left\{ \prod_{i=1}^d \sin(x_i)^{a_i} \prod_{i=1}^d \cos(x_i)^{b_i} \mid a_i, b_i \in \llbracket 0, 1 \rrbracket, i \in \llbracket 1, d \rrbracket, 0 \leq \sum_{i=1}^d (a_i + b_i) \leq 2 \right\}.$$

Which has a cardinality of $1 + d + 2d^2$. Note however, that the data is contaminated with noise, and so we observe \mathbf{y} as opposed to \mathbf{x} . For the system we choose the natural frequency $\omega_i \sim \mathcal{U}[0, 1]$ for $i \in \llbracket 1, d \rrbracket$. The random starting point for each instance of the experimental data used is chosen as $\mathbf{x}^j(t_0) \sim \mathcal{U}[0, 2\pi]^d$. This starting point is used to generate a trajectory according to the exact dynamic using a high-order Runge-Kutta scheme for a maximum time $t_{T/c}$ of 10 seconds. This trajectory is then contaminated with noise, in accordance with the description in the previous section.

Remark 4.9. Note that if we were to include $\cos(y_i)^2$ and $\sin(y_i)^2$ for $i \in \llbracket 1, d \rrbracket$ in \mathcal{D} , the matrix $\Psi(Y)$ built with this library would not have full rank, as $\cos(y_i)^2 + \sin(y_i)^2 = 1$, and the library \mathcal{D} already includes a built-in constant. In our experiments we have observed that when using a dictionary that does not have full rank, the thresholded least-squares algorithm SINDy tends to produce solutions that include constant, $\cos(y_i)^2$ and $\sin(y_i)^2$ terms, whereas the dynamics returned by the CINDy algorithm tends to only include constant terms, thereby providing a more parsimonious representation of the dynamic. If we add an ℓ_2 regularization term to the optimization algorithm, resulting in a thresholded ridge regression algorithm, the resulting dynamic tends toward higher parsimony, but at the expense of accuracy in predicting derivatives and trajectories.

We also test the performance of the CINDy algorithm and the IPM algorithm with the addition of symmetry constraints. We use $\xi_j(\psi(\mathbf{x}))$ to refer to the coefficient in ξ_j , where ξ_j is the j -th column of Ξ , associated with the basis function $\psi(\mathbf{x})$. The underlying rationale behind the constraints is that as the particles are identical, except for their intrinsic frequency, the effect of x_i on x_j should be the same as the effect of x_j on x_i . In both the integral and the differential formulation we impose that for all $i, j \in \llbracket 1, d \rrbracket$:

$$\begin{aligned}\xi_j(\sin(x_i)) &= \xi_i(\sin(x_j)) \\ \xi_i(\cos(x_i)) &= \xi_i(\cos(x_j)) \\ \xi_j(\cos(x_i)) &= \xi_i(\cos(x_j)) \\ \xi_j(\sin(x_i)\cos(x_j)) &= \xi_i(\sin(x_j)\cos(x_i)) \\ \xi_j(\cos(x_i)\sin(x_j)) &= \xi_i(\cos(x_j)\sin(x_i)) \\ \xi_j(\sin(x_i)\sin(x_j)) &= \xi_i(\sin(x_j)\sin(x_i)) \\ \xi_j(\cos(x_i)\cos(x_j)) &= \xi_i(\cos(x_j)\cos(x_i)),\end{aligned}$$

which are simple linear constraints that can easily be added to the linear optimization oracle used in Line 7 of the CINDy algorithm (Algorithm 3).

The images in Figure 3 and 4 show the recovery results for $K = 2$ and $h = 0.2$ and two different values for the dimension, $d = 5$ and $d = 10$, respectively. A total of 6000 points were used to infer the dynamic, spread over 40 experiments for a maximum time of 10 seconds, for both cases. The values of the noise level α ranged from 10^{-8} to 10^{-2} . The derivatives used were computed using differentiation of local polynomial approximations, and the integrals using integration of local polynomial approximations. Each test was performed 20 times. The graphs indicate with lines the average value obtained with \mathcal{E}_R , \mathcal{E}_D and \mathcal{E}_T , \mathcal{S}_E and \mathcal{S}_E for a given noise level and algorithm. The shaded regions indicate the value obtained after adding and subtracting a standard deviation to the average error for each noise level and algorithm.

For the case with $d = 5$ (see Figure 3) we can observe that in the differential formulation the CINDy, CINDy (c) and SINDy algorithms achieve the smallest recovery error \mathcal{E}_R for noise levels below 10^{-4} , and the performance of the SINDy algorithm degrades after that, relative to that of the best-performing algorithms. Whereas the CINDy and CINDy (c) algorithms are among the best performing in terms of \mathcal{E}_R for all noise levels. Regarding the \mathcal{E}_D and \mathcal{E}_T errors, there is no clear distinction between the algorithms. Regarding the sparsity achieved through the algorithms, we can see that CINDy and CINDy (c) consistently tend to produce the sparsest solutions, as measured with \mathcal{S}_E , whereas IPM and IPM (c) tend to pick up all the terms in the dictionary. For interior point methods, dense solutions are of course to be expected if no solution rounding is performed. Note also that the performance of SINDy degrades above a noise level of 10^{-4} , where it starts to produce dense solutions. Lastly, on average none of the algorithms tends to miss more than one of the basis functions that are present in the exact dynamic, as measured by \mathcal{S}_M , this is especially remarkable for the CINDy and CINDy (c) algorithms, which consistently have the lowest number of extra terms. Overall, in the differential formulation experiments we observe that the CINDy and CINDy (c) algorithms produce the most accurate solutions, as measured by \mathcal{E}_R , consistently producing among the best dynamics for all the noise levels, while producing dynamics that are much sparser than the ones produced by in general.

In terms of integral formulation, the CINDy and CINDy (c) algorithms are on average more accurate in terms of \mathcal{E}_R than any of the algorithms tested, by a larger margin than in the differential formulation. Regarding the \mathcal{E}_D and \mathcal{E}_T error, as in the results for the differential formulation, there are only slight differences between the method. However, the CINDy and CINDy (c) algorithms produce the sparsest solutions, with all the remaining algorithms picking up a large number of extraneous basis functions.

For the case with $d = 10$ (see Figure 4) in the differential case, we can see very good performance from the SINDy, CINDy, CINDy (c), and FISTA algorithms in \mathcal{E}_R for noise levels below 10^{-5} . However, the performance for SINDy degrades above 10^{-5} , in terms of recovery accuracy (there is a difference of more than two orders of magnitude between SINDy and CINDy), and in terms of \mathcal{S}_E , as the algorithm starts picking up most of the available basis functions from the dictionary. The performance of the FISTA algorithm degrades above 10^{-3} , also in terms of \mathcal{E}_R and \mathcal{S}_E . Regarding the integral formulation, there is a large difference in the performance of CINDy and CINDy (c), and the rest of the algorithms. For most noise levels

these two aforementioned algorithms are more than two orders of magnitude more accurate in terms of \mathcal{E}_R , while maintaining extremely sparse solutions. This performance difference is key in accurately simulation out-of-sample trajectories. Regarding the IPM and IPM (c) results, we were not able to get the performance of these two algorithms to be on par with the other algorithms for low noise levels, despite increasing the accuracy of the solver.

4.2.1 SAMPLE EFFICIENCY

One of the most crucial aspects of many modern learning problems is the quantity of data needed to train a given model to achieve a certain target accuracy. When training data is expensive to gather, it is usually advantageous to use models or frameworks that require the least amount of training data to reach a given target accuracy on validation data. As we can see in Figure 3, in both the differential and integral formulation all the algorithms perform similarly when tested on noisy validation data, as is shown in the second and third rows of images, however, there are disparities in how they perform when measuring the performance against the exact dynamic, as seen in the first row of images. For example, in the differential formulation the CINDy and CINDy (c) algorithms perform noticeably better than the SINDy algorithm for higher noise levels, from 10^{-4} to 10^{-2} , and in the integral formulation the CINDy and CINDy (c) algorithms perform noticeably better than the SINDy algorithm for noise levels below 10^{-3} . From a sample efficiency perspective, this suggests that in both these regimes where CINDy has an advantage, it will require fewer samples than SINDy to reach a target accuracy.

This is confirmed in Figure 5, which shows a heat map of $\log(\mathcal{E}_R)$ for different noise levels (x-axis) and different numbers of training samples (y-axis), when using the Kuramoto model of dimension $d = 5$ for benchmarking. If one takes a look at the differential formulation, one can see that in the low training sample regime both CINDy and CINDy (c) perform better than SINDy at higher noise levels. It should also be noted that CINDy (c) performs better than CINDy, which is expected, as the introduction of extra constraints *lowers the dimensionality* of our learning problem, for which we now have to learn fewer parameters. Thus the addition of constraints brings two advantages: (1) it outputs dynamics that are consistent with the underlying physics of the phenomenon and (2) it can potentially require fewer data samples to train. Similar conclusions can be drawn when inspecting the results for the integral formulation, for example focusing again on the low training sample regime. We provide an extended analysis over a broader range of sample sizes in Appendix E for completeness.

4.2.2 SIMULATION OF LEARNED TRAJECTORIES

By observing the results for \mathcal{E}_T in Figure 4 it would seem at first sight that all the algorithms (except the IPM and IPM (c) algorithms for low noise levels) will perform similarly when inferring trajectories from an initial position. However, when we simulate the Kuramoto system from a given initial position, the algorithms have very different performances. This is due to the fact that while the single point evaluations might have rather similar errors (on average), which means nothing else but that they generalize similarly on the specific evaluations (as expected as this was the considered objective function) they do differ very much in their *structural generalization behavior*: all algorithms but CINDy and CINDy (c) pick up wrong terms to explain the dynamic, which then in the trajectory evolution, due to compounding, lead to significant mismatches.

In Figure 6 we show the results after simulating the dynamics learned by the CINDy and SINDy algorithm from the integral formulation for a Kuramoto model with $d = 10$ and a noise level of 10^{-3} . In order to see more easily the differences between the algorithms and the position of the oscillators, we have placed the i -th oscillator at a radius of i , for $i \in \llbracket 1, d \rrbracket$. This is contrary to how this dynamic is usually visualized, with all the particles oscillating with the same radii.

4.3 Fermi-Pasta-Ulam-Tsingou model

The Fermi-Pasta-Ulam-Tsingou model describes a one-dimensional system of d identical particles, where neighboring particles are connected with springs, subject to a nonlinear forcing term (Fermi et al., 1955). This computational model was used at Los Alamos to study the behaviour of complex physical systems over

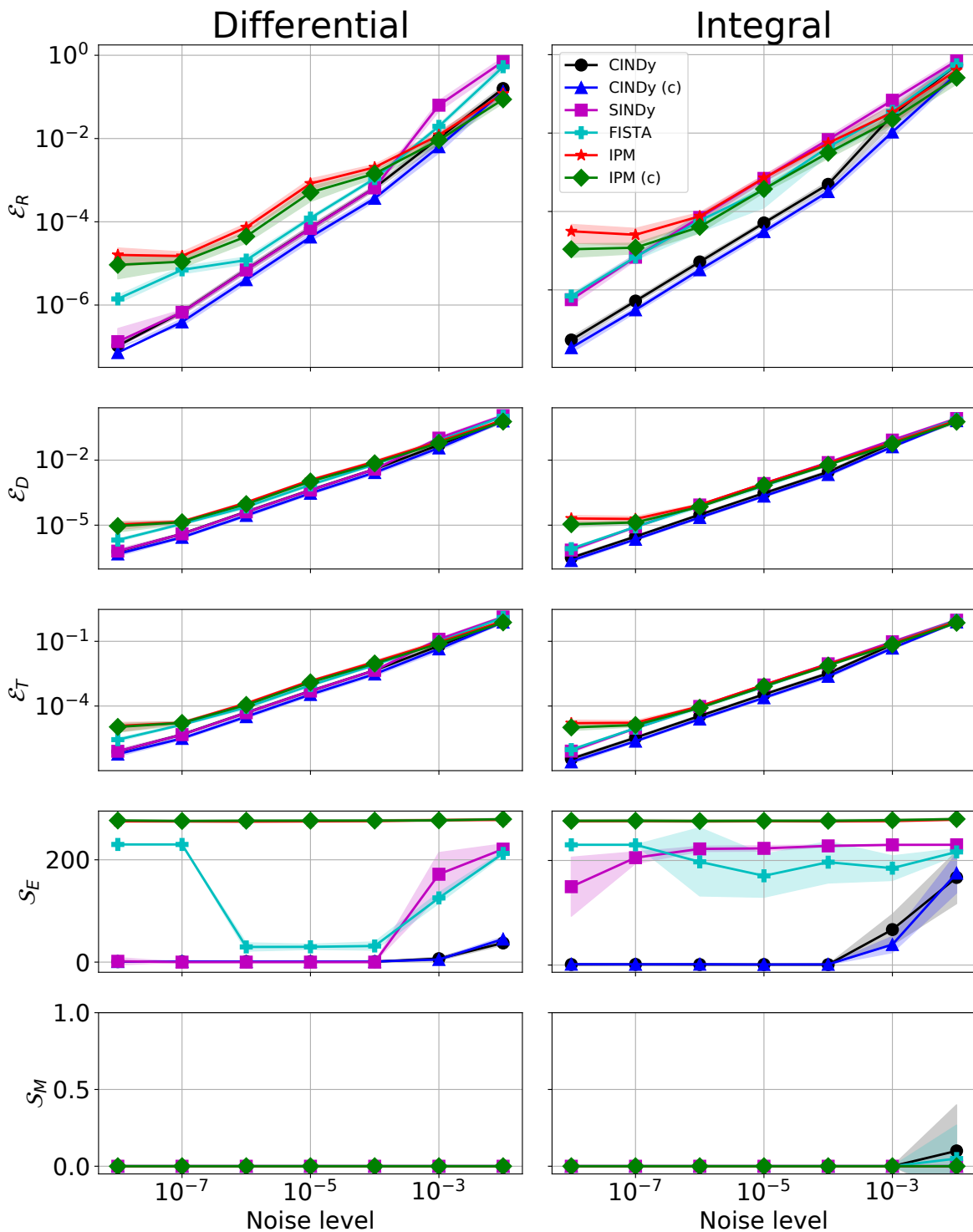


Figure 3: **Sparse recovery of the Kuramoto model:** Algorithm comparison for a Kuramoto model of dimension $d = 5$, with a differential formulation shown on the left column, and with an integral formulation on the right column. The first, second, third, fourth and fifth rows of images indicate a comparison of \mathcal{E}_R , \mathcal{E}_D , \mathcal{E}_T , S_E , and S_M , as we vary the noise level, respectively.

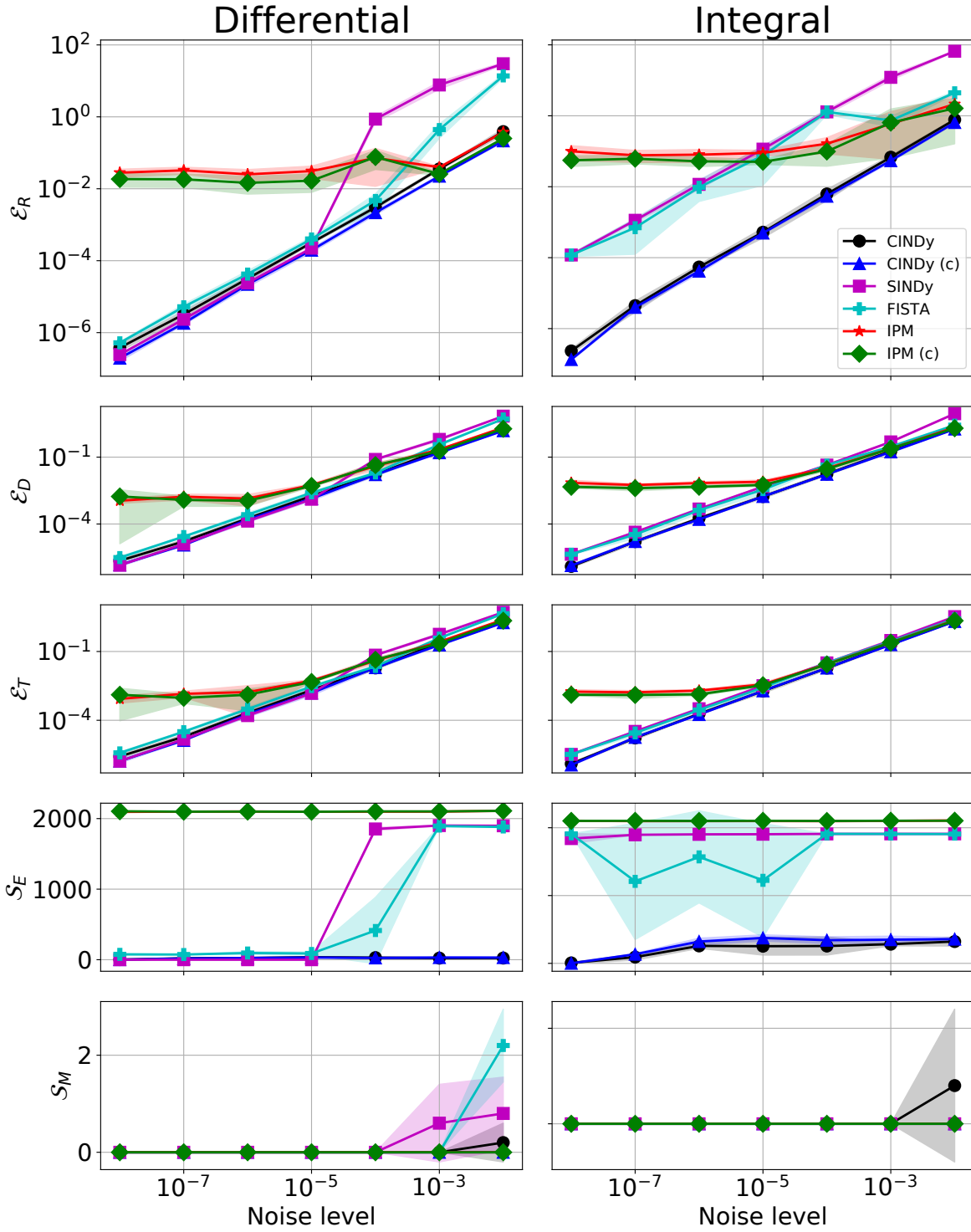


Figure 4: **Sparse recovery of the Kuramoto model:** Algorithm comparison for a Kuramoto model of dimension $d = 10$, with a differential formulation shown on the left column, and with an integral formulation on the right column. The first, second, third, fourth and fifth rows of images indicate a comparison of ε_R , ε_D , ε_T , S_E , and S_M , as we vary the noise level, respectively.

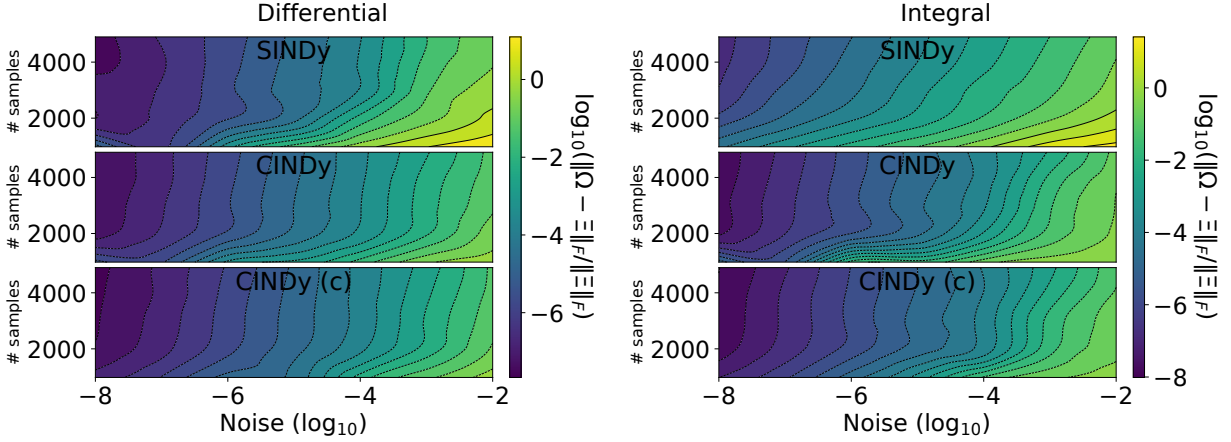


Figure 5: **Sample efficiency of the sparse recovery of the Kuramoto model:** Algorithm comparison for a Kuramoto model of dimension $d = 5$ for both formulations shown in Figures (a), (b).

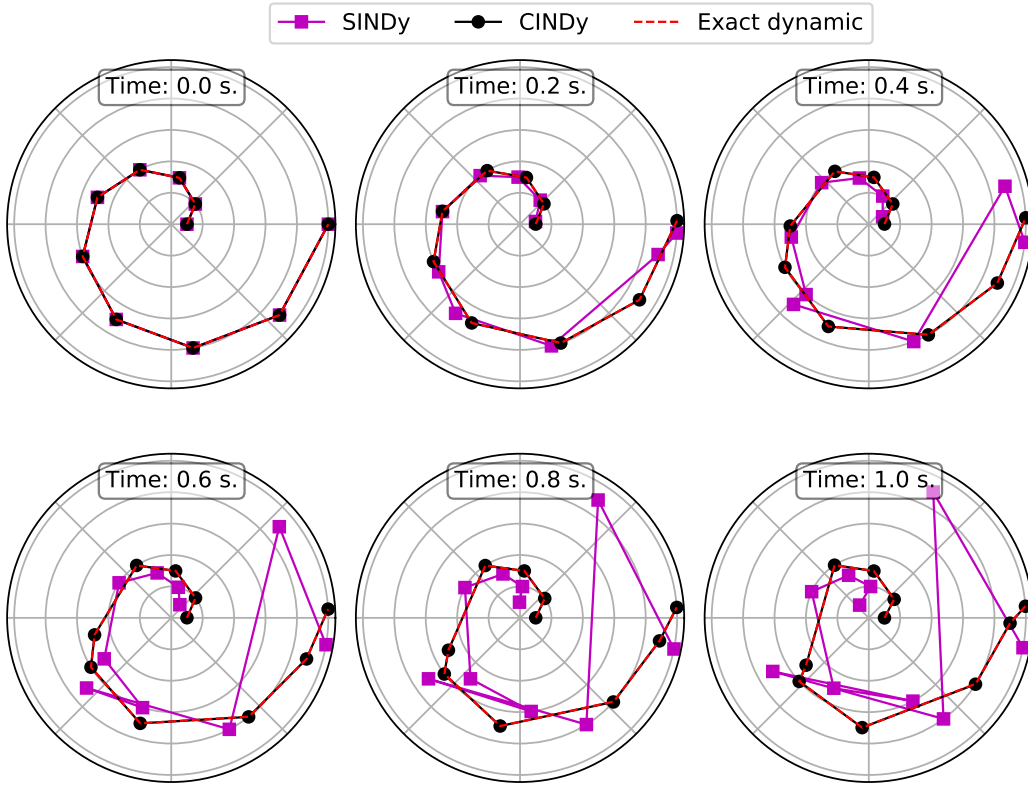


Figure 6: **Trajectory comparison:** Kuramoto model of dimension $d = 10$.

long time periods. The prevailing hypothesis behind the experiments was the idea that these systems would eventually exhibit ergodic behaviour, as opposed to the approximately periodic behaviour that some complex physical systems seemed to exhibit. This is indeed the case, as this model transitions to an ergodic behaviour, after seemingly periodic behaviour over the short time scale. This dynamic has already been used in [Gelf et al. \(2019\)](#). The equations of motion that govern the particles, when subjected to cubic forcing terms is

given by

$$\ddot{x}_i = (x_{i+1} - 2x_i + x_{i-1}) + \beta [(x_{i+1} - x_i)^3 - (x_i - x_{i-1})^3],$$

where $i \in \llbracket 1, d \rrbracket$ and x_i refers to the displacement of the i -th particle with respect to its equilibrium position. The exact dynamic Ξ can be expressed using a dictionary of monomials of degree up to three. To be more precise, the dictionary used is:

$$\mathcal{D} = \left\{ \prod_{i=1}^d x_i^{a_i} \mid a_i \in \llbracket 0, 3 \rrbracket, i \in \llbracket 1, n \rrbracket, 0 \leq \sum_{i=1}^d a_i \leq 3 \right\},$$

which has cardinality $\binom{d+3}{3}$. Using this dictionary we know that the exact dynamic satisfies $\|\Psi\|_0 = 10d - 8$. As in the previous example, we can impose a series of linear constraints between the dynamics of neighboring particles (as the particles are identical). In both the integral and the differential formulation we impose that for all $i \in \llbracket 1, d \rrbracket$ and all $j \in \{i+1, i-1\}$ with $0 \leq j \leq d$,

$$\xi_j (x_i^a x_j^b) = \xi_i (x_i^b x_j^a)$$

holds with $a, b \in \llbracket 1, 3 \rrbracket$ and $0 \leq a + b + c \leq 3$.

Remark 4.10 (On the construction of \ddot{Y} and $\delta\dot{Y}$). In this case we are dealing with a second-order ordinary differential equation (ODE), as opposed to a first-order ODE. As we only have access to noisy measurements $\{\mathbf{y}(t_i)\}_{i=1}^m$, if we are dealing with the differential formulation, we have to numerically estimate $\{\ddot{\mathbf{y}}(t_i)\}_{i=1}^m$, in order to solve

$$\underset{\substack{\Omega \in \mathcal{P} \\ \Omega \in \mathbb{R}^{n \times d}}}{\operatorname{argmin}} \|\ddot{Y} - \Omega^T \Psi(Y)\|_F^2,$$

where $\ddot{Y} = [\ddot{\mathbf{y}}(t_1), \dots, \ddot{\mathbf{y}}(t_m)] \in \mathbb{R}^{d \times m}$ is the matrix with the estimates of the second derivatives of \mathbf{y} with respect to time as columns. On the other hand, if we wish to tackle the problem from an integral perspective, we now use the fact that $\dot{\mathbf{x}}(t_{i+1}) = \dot{\mathbf{x}}(t_1) + \int_{t_1}^{t_{i+1}} \Xi^T \psi(\mathbf{x}(\tau)) d\tau$, which allows us to phrase the sparse regression problem from an integral perspective as

$$\underset{\substack{\Omega \in \mathcal{P} \\ \Omega \in \mathbb{R}^{n \times d}}}{\operatorname{argmin}} \|\delta\dot{Y} - \Omega^T \Gamma(Y)\|_F^2,$$

where $\delta\dot{Y} = [\dot{\mathbf{y}}(t_2) - \dot{\mathbf{y}}(t_1), \dots, \dot{\mathbf{y}}(t_m) - \dot{\mathbf{y}}(t_1)] \in \mathbb{R}^{d \times m-1}$ and $\Gamma(Y)$ is computed similarly as in Section 2. Note that in this case using the differential formulation requires estimating the second derivative of the noisy data with respect to time to form \ddot{Y} , whereas the integral formulation requires estimating the first derivative with respect to time to form $\delta\dot{Y}$.

The images in Figure 7 and 8 show the recovery results for $d = 5$ and $d = 10$, respectively, when learning the Fermi-Pasta-Ulam-Tsingou with $\beta = 0.7$. The exact dynamic in this case satisfies $\|\Xi\|_0 = 42$ and $\|\Xi\|_0 = 92$ for $d = 5$ and $d = 10$, respectively. In the lower dimensional experiment we used 4500 points, and in the higher dimensional one 9000. In both cases we spread out the points across 150 experiments, for a maximum time of 1 second per experiment. The derivatives used were computed using polynomial interpolation of degree 8. We used polynomial interpolation of degree 8 to compute the integrals for all the noise levels. The values of the noise level α ranged from 10^{-8} to 10^{-2} . Each test was performed 20 times. The graphs indicate with lines the average value obtained with \mathcal{E}_R , \mathcal{E}_D and \mathcal{E}_T , \mathcal{S}_E and \mathcal{S}_M for a given noise level and algorithm. The shaded regions indicate the value obtained after adding and subtracting a standard deviation to the average error for each noise level and algorithm.

For the case with $d = 5$ (Figure 7) we can observe that in both the differential and integral formulation all the algorithms perform similarly in terms \mathcal{E}_D and \mathcal{E}_T , however, we can see that the CINDy and CINDy (c) algorithms perform better or on par with the best performing algorithm. For low noise levels the CINDy

algorithm performs 2-5 times better than the worst performing algorithm. There is a huge difference in the number of extra basis functions picked up by the algorithms, as measured by \mathcal{S}_E , as the CINDy and CINDy (c) do not pick up any extra basis functions until the noise level is above 10^{-5} , whereas all the other algorithms, with the exception of the SINDy algorithm for a noise level of 10^{-8} , pick up extra vertices. The IPM and IPM (c) algorithms tend to pick up all the possible basis functions, as does the SINDy algorithm for noise levels above 10^{-6} . Note how for small noise levels the SINDy algorithm does not pick up a significant amount of extra basis functions in the differential formulation, and with an increase in the noise level the SINDy algorithms tends to pick up all the available ansatz. As the SINDy, IPM and IPM (c) tend to approximately pick up all the available basis functions for noise levels above 10^{-6} , they consequently do not miss out any basis functions, as measured by \mathcal{S}_M . The FISTA, CINDy and CINDy (C) algorithms miss out on some of the basis functions at higher noise levels, due to the fact that they have a higher tendency towards producing sparse solutions.

For the case with $d = 10$ (Figure 8) we observe again that all the models perform similarly in terms of \mathcal{E}_D and \mathcal{E}_T in both the integral and differential formulation. However, the difference between the algorithms in terms of \mathcal{E}_R is magnified. For example, the CINDy, CINDy (c) and FISTA algorithms are up to two orders of magnitude more accurate than the SINDy algorithm in terms of \mathcal{E}_R for the differential formulation. They also provide the sparsest solutions in terms of \mathcal{S}_E . In the integral formulation the CINDy and CINDy (c) algorithms are also two orders of magnitude more accurate than SINDy. The LASSO algorithm performs better than SINDy, but significantly worse than CINDy and CINDy (c) in terms of \mathcal{E}_R . In terms of performance with respect to \mathcal{S}_E the CINDy and CINDy significantly better than the other algorithms, however for the highest noise levels they miss out on a significant number of basis functions, as measured by \mathcal{S}_M . For all noise levels except in one, the SINDy algorithm tends to pick up all the available basis functions, as can be seen in the plot for \mathcal{S}_E .

4.3.1 SIMULATION OF LEARNED TRAJECTORIES

The results shown in Figure 8 for \mathcal{E}_T (see third row of images) seem to indicate that all four formulations will perform similarly when predicting trajectories, however, this stands in contrast to what is shown in the first row of images, where we can see that the dynamic learned by SINDy is far from the true dynamic. This discrepancy is due to the fact that all the data is generated in one regime of the dynamical phenomenon, and the metric \mathcal{E}_T is computed using noisy testing data from the same regime. If we were to test the performance in inferring trajectories with initial conditions that differed from those that had been seen in the training-testing-validation data, the picture would be quite different. For example one could test the inference power of the different dynamics if the initial position of the oscillators is a sinusoid with unit amplitude.

We can see the difference in accuracy between the different learned dynamics by simulating forward in time the dynamic learned by the CINDy algorithm and the SINDy algorithm, and comparing that to the evolution of the true dynamic. The results in Figure 9 show the difference in behaviour for different times for the dynamics learnt by the two algorithms in the integral formulation with a noise level of 10^{-4} for the example of dimensionality $d = 10$. In keeping with the physical nature of the problem, we present the ten dimensional phenomenon as a series of oscillators suffering a displacement on the vertical y-axis, in a similar fashion as was done in the original paper (Fermi et al., 1955). Note that we have added to the images the two extremal particles that do not oscillate.

The two orders of magnitude in difference between the SINDy and the CINDy algorithms, in terms of \mathcal{E}_R , manifests itself clearly when we try to predict trajectories with out-of-sample initial positions that differ from those that have been used for learning. This suggests that the CINDy algorithm has better generalization properties under noise.

4.4 Michaelis-Menten model

The Michaelis-Menten model is used to describe enzyme reaction kinetics (Michaelis & Menten, 2007). We focus on the following derivation (Briggs & Haldane, 1925), in which an enzyme E combines with a substrate S to form an intermediate product ES with a reaction rate k_f . This reaction is reversible, in the sense that

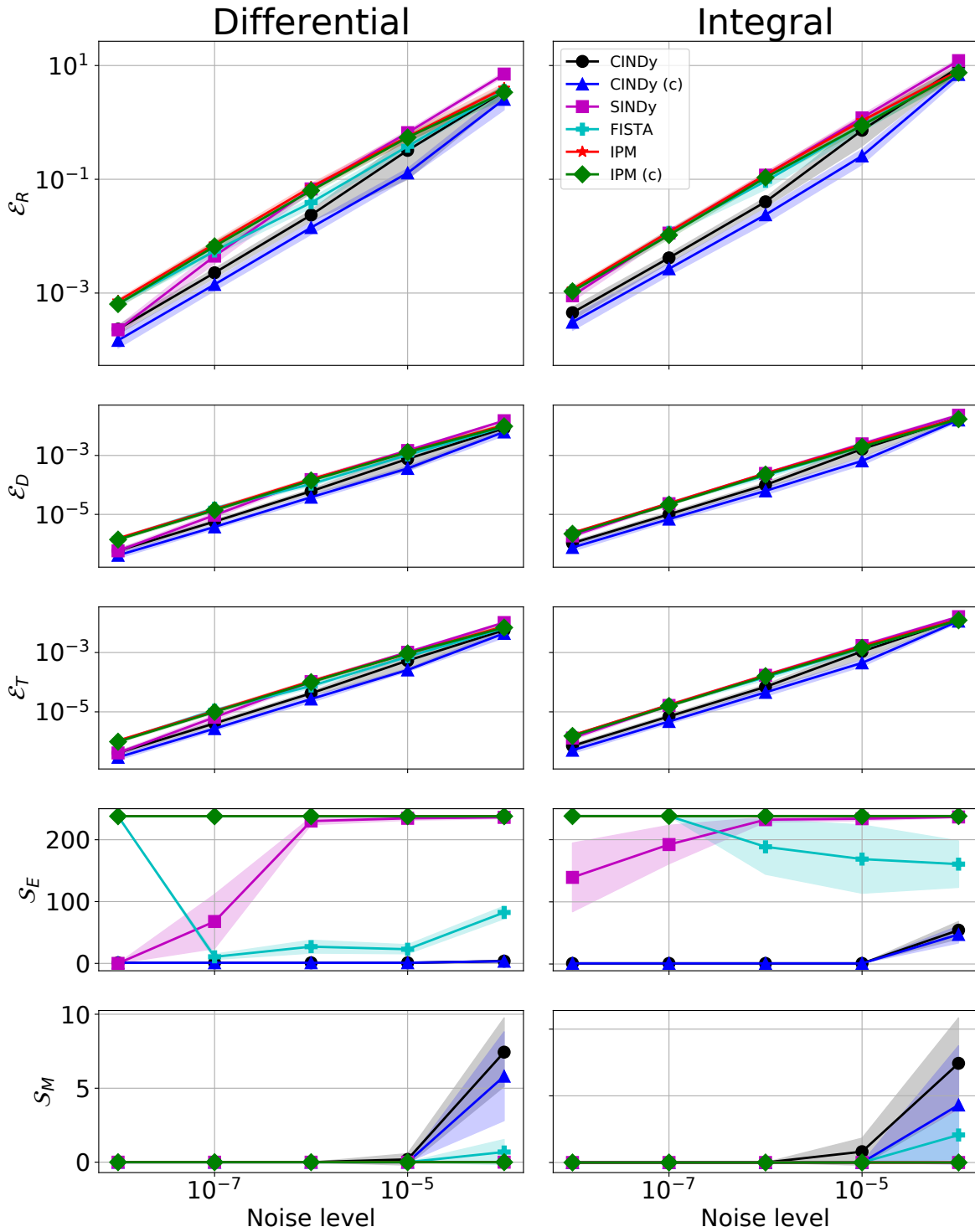


Figure 7: **Sparse recovery of the Fermi-Pasta-Ulam-Tsingou model:** Algorithm comparison for a Fermi-Pasta-Ulam-Tsingou model of dimension $d = 5$, with a differential formulation shown on the left column, and with an integral formulation on the right column. The first, second, third, fourth and fifth rows of images indicate a comparison of \mathcal{E}_R , \mathcal{E}_D , \mathcal{E}_T , \mathcal{S}_E , and \mathcal{S}_M , as we vary the noise level, respectively.

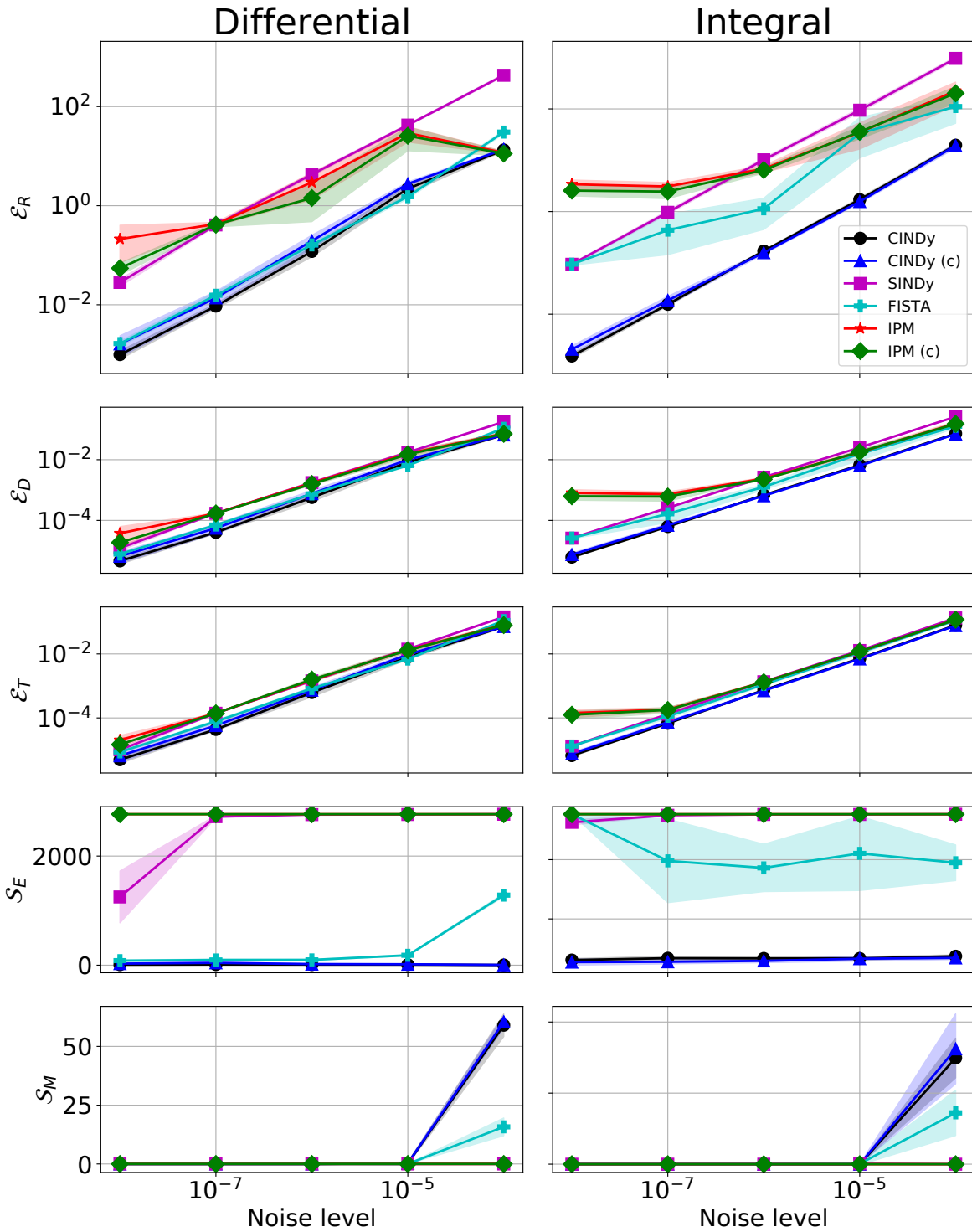


Figure 8: **Sparse recovery of the Fermi-Pasta-Ulam-Tsingou model:** Algorithm comparison for a Fermi-Pasta-Ulam-Tsingou model of dimension $d = 10$, with a differential formulation shown on the left column, and with an integral formulation on the right column. The first, second, third, fourth and fifth rows of images indicate a comparison of \mathcal{E}_R , \mathcal{E}_D , \mathcal{E}_T , \mathcal{S}_E , and \mathcal{S}_M , as we vary the noise level, respectively.

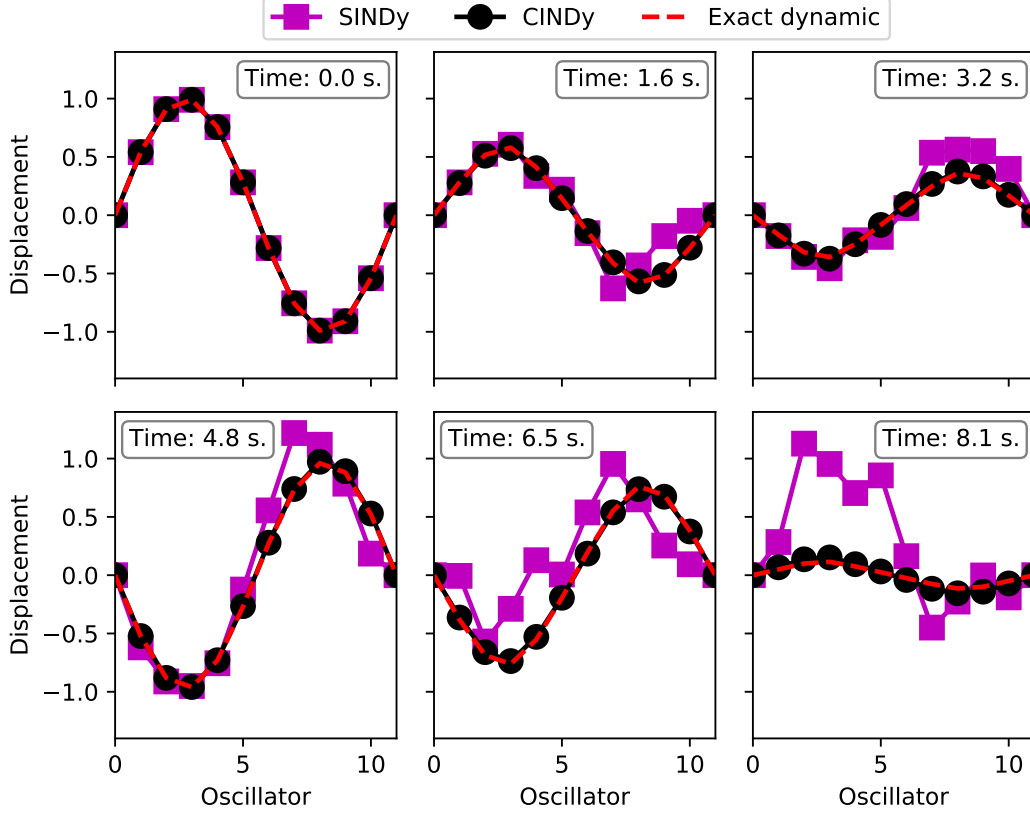


Figure 9: **Trajectory comparison:** Fermi-Pasta-Ulam-Tsingou model of dimension $d = 10$.

the intermediate product ES can decompose into E and S, with a reaction rate k_r . This intermediate product ES can also proceed to form a product P, and regenerate the free enzyme E. This can be expressed as



If we assume that the rate for a given reaction depends proportionately on the concentration of the reactants, and we denote the concentration of E, S, ES and P as x_E , x_S , x_{ES} and x_P , respectively, we can express the dynamics of the chemical reaction as:

$$\begin{aligned} \dot{x}_E &= -k_f x_E x_S + k_r x_{ES} + k_{cat} x_{ES} \\ \dot{x}_S &= -k_f x_E x_S + k_r x_{ES} \\ \dot{x}_{ES} &= k_f x_E x_S - k_r x_{ES} - k_{cat} x_{ES} \\ \dot{x}_P &= k_{cat} x_{ES}. \end{aligned}$$

One of the interesting things about the Michaelis-Menten dynamic is that we can use some of the structural constraints described in Section 2.1.1, that is, the exact dynamic satisfies

$$\begin{aligned} \dot{x}_S + \dot{x}_{ES} + \dot{x}_P &= 0 \\ \dot{x}_E + \dot{x}_{ES} &= 0. \end{aligned}$$

The exact dynamic Ξ can be expressed using a dictionary of monomials of degree up to two. To be more precise, the dictionary used is

$$\mathcal{D} = \{x_E^{a_E} x_S^{a_S} x_{ES}^{a_{ES}} x_P^{a_P} \mid a_E, a_S, a_{ES}, a_P \in \llbracket 0, 2 \rrbracket, 0 \leq a_E + a_S + a_{ES} + a_P \leq 2\}.$$

With this dictionary in mind, and denoting the coefficient vector associated with the chemical E as ξ_E , and likewise for the other chemicals, we can impose the following additional series of constraints for all i :

$$\begin{aligned}\xi_E + \xi_S + \xi_P &= 0 \\ \xi_E + \xi_{ES} &= 0.\end{aligned}$$

The images in Figure 10 show the recovery results for $k_f = 0.01$, $k_r = 1$, $k_{\text{cat}} = 1$ and $d = 4$. The derivatives used were computed using a polynomial interpolation of degree 8. We used polynomial interpolation of degree 8 to compute the integrals for all the noise levels. A total of 6000 points were used to infer the dynamic, spread over 150 experiments for a maximum time of 0.01 seconds, for both cases. The initial state of the system for the j -th experiment was selected randomly as $\mathbf{x}^j(t_0) \sim \mathcal{U}[0, 1]^4$.

As in the previous experiment, in both the differential and integral formulation, all the algorithms perform similarly in terms of \mathcal{E}_D and \mathcal{E}_T . For noise levels below 10^{-3} there is a clear benefit to using the CINDy and CINDy (c) algorithms, as these are up to an order of magnitude more accurate than the other algorithms in terms of \mathcal{E}_R . For noise levels above 10^{-3} the CINDy and CINDy (c) algorithms perform similarly to the other algorithms in terms of \mathcal{E}_R . As in the previous examples, there is also a huge difference in the number of extra basis functions picked up, as measured by \mathcal{S}_E , with CINDy producing in general the sparsest solutions, followed by FISTA and CINDy (c) (although the latter has the added benefit that it preserves some of the structure behind the physical phenomenon due to the constraints). The IPM, IPM (c) and SINDy algorithms tend to pick up all the available basis functions for noise levels above 10^{-6} . In terms of correct basis functions that have not been picked up, the FISTA, CINDy and CINDy (c) algorithms only miss out on average on less than one of the basis functions for the highest noise levels in the differential formulation. Similar comments can be made regarding the integral formulation, where we observe that the aforementioned three algorithms only miss out on some basis functions for noise levels above 10^{-2} .

Acknowledgments

This research was partially funded by Deutsche Forschungsgemeinschaft (DFG) through the DFG Cluster of Excellence MATH+.

References

- Acebrón, J. A., Bonilla, L. L., Vicente, C. J. P., Ritort, F., and Spigler, R. The Kuramoto model: A simple paradigm for synchronization phenomena. *Reviews of modern physics*, 77(1):137, 2005.
- Andersen, M., Dahl, J., Liu, Z., Vandenberghe, L., Sra, S., Nowozin, S., and Wright, S. Interior-point methods for large-scale cone programming. *Optimization for machine learning*, 5583, 2011.
- Beck, A. and Teboulle, M. A fast iterative shrinkage-thresholding algorithm for linear inverse problems. *SIAM journal on imaging sciences*, 2(1):183–202, 2009.
- Borwein, J. and Lewis, A. S. *Convex analysis and nonlinear optimization: theory and examples*. Springer Science & Business Media, 2010.
- Braun, G., Pokutta, S., Tu, D., and Wright, S. Blended conditional gradients. In *International Conference on Machine Learning*, pp. 735–743. PMLR, 2019.
- Braun, G., Carderera, A., Combettes, C. W., Hassani, H., Karbasi, A., Mokhtari, A., and Pokutta, S. Conditional gradients - a survey. *Forthcoming*, 2021.
- Briggs, G. E. and Haldane, J. B. S. A note on the kinetics of enzyme action. *Biochemical journal*, 19(2): 338–339, 1925.

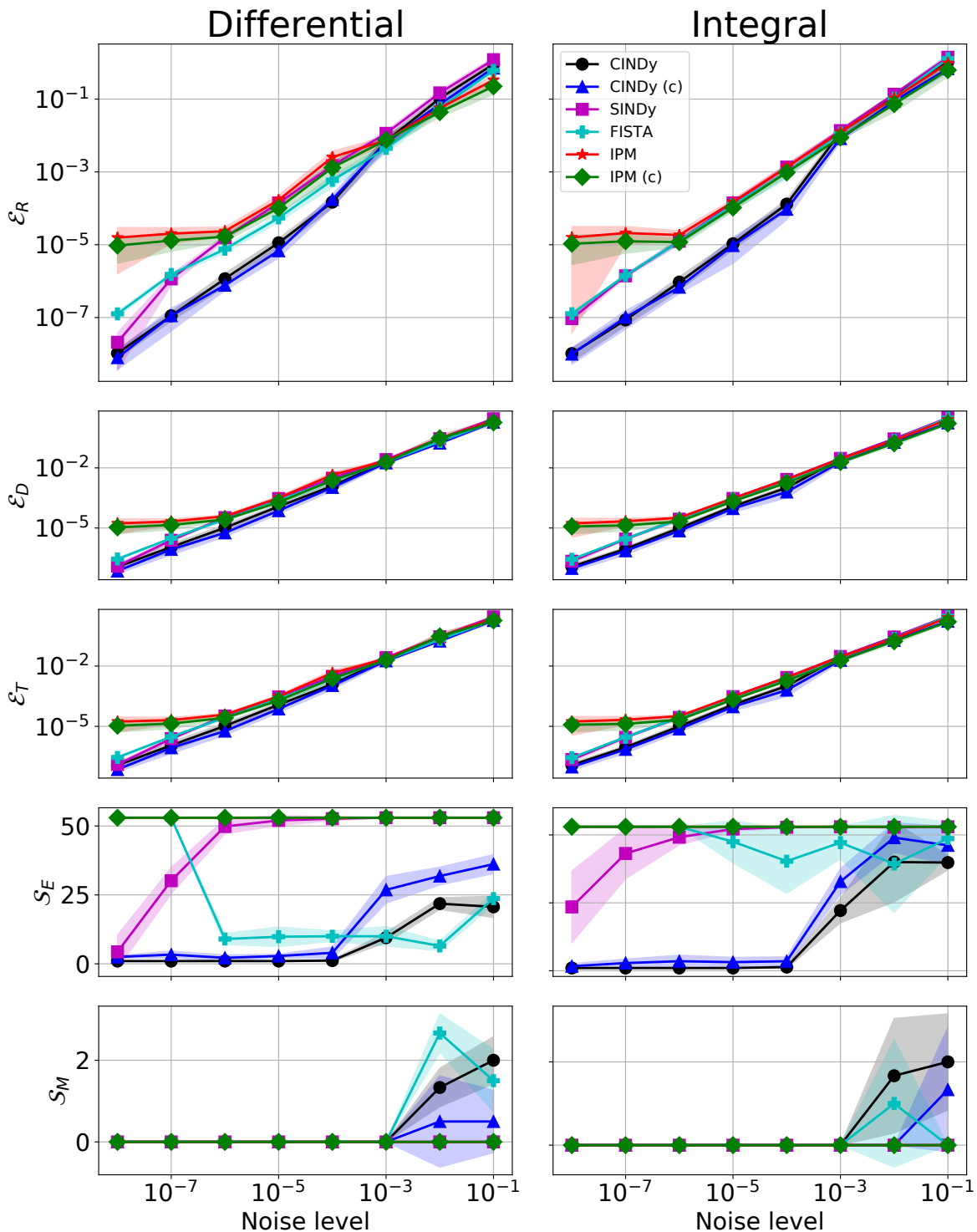


Figure 10: **Sparse recovery of the Michaelis-Menten model:** Algorithm comparison for a Michaelis-Menten model of dimension $d = 4$, with a differential formulation shown on the left column, and with an integral formulation on the right column. The first, second, third, fourth and fifth rows of images indicate a comparison of ϵ_R , ϵ_D , ϵ_T , S_E , and S_M , as we vary the noise level, respectively.

- Brunton, S. L., Proctor, J. L., and Kutz, J. N. Discovering governing equations from data by sparse identification of nonlinear dynamical systems. *Proceedings of the national academy of sciences*, 113(15): 3932–3937, 2016.
- Candès, E. J., Romberg, J., and Tao, T. Robust uncertainty principles: Exact signal reconstruction from highly incomplete frequency information. *IEEE Transactions on information theory*, 52(2):489–509, 2006.
- Champion, K., Lusch, B., Kutz, J. N., and Brunton, S. L. Data-driven discovery of coordinates and governing equations. *Proceedings of the National Academy of Sciences*, 116(45):22445–22451, 2019. ISSN 0027-8424. doi: 10.1073/pnas.1906995116. URL <https://www.pnas.org/content/116/45/22445>.
- Champion, K., Zheng, P., Aravkin, A. Y., Brunton, S. L., and Kutz, J. N. A unified sparse optimization framework to learn parsimonious physics-informed models from data. *IEEE Access*, 8:169259–169271, 2020.
- Chen, S. S., Donoho, D. L., and Saunders, M. A. Atomic decomposition by basis pursuit. *SIAM Journal on Scientific Computing*, 20(1):33–61, 1998.
- Combettes, P. L. and Pesquet, J.-C. Proximal splitting methods in signal processing. In *Fixed-point algorithms for inverse problems in science and engineering*, pp. 185–212. Springer, 2011.
- Condat, L. Fast projection onto the simplex and the ℓ_1 ball. *Mathematical Programming*, 158(1-2):575–585, 2016.
- Fermi, E., Pasta, P., Ulam, S., and Tsingou, M. Studies of the nonlinear problems. Technical report, Los Alamos Scientific Lab., N. Mex., 1955.
- Foucart, S. and Rauhut, H. A mathematical introduction to compressive sensing. *Bull. Am. Math.*, 54:151–165, 2017.
- Frank, M. and Wolfe, P. An algorithm for quadratic programming. *Naval Research Logistics Quarterly*, 3(1-2):95–110, 1956.
- Gelß, P., Klus, S., Eisert, J., and Schütte, C. Multidimensional approximation of nonlinear dynamical systems. *Journal of Computational and Nonlinear Dynamics*, 14(6), 2019.
- Hanke, M. Accelerated landweber iterations for the solution of ill-posed equations. *Numer. Math.*, 60:341–373, 1991.
- Heldt, D., Kreuzer, M., Pokutta, S., and Poulisse, H. Approximate computation of zero-dimensional polynomial ideals. *Journal of Symbolic Computation*, 44(11):1566–1591, 2009.
- Hoffmann, M., Fröhner, C., and Noé, F. Reactive sindy: Discovering governing reactions from concentration data. *The Journal of Chemical Physics*, 150(2):025101, 2019.
- Juditsky, A. and Nemirovski, A. *Statistical Inference via Convex Optimization*, volume 69. Princeton University Press, 2020.
- Kaheman, K., Brunton, S. L., and Kutz, J. N. Automatic differentiation to simultaneously identify nonlinear dynamics and extract noise probability distributions from data. *arXiv preprint arXiv:2009.08810*, 2020.
- Knowles, I. and Renka, R. J. Methods for numerical differentiation of noisy data. *Electron. J. Differ. Equ.*, 21:235–246, 2014.
- Kuramoto, Y. Self-entrainment of a population of coupled non-linear oscillators. In *International symposium on mathematical problems in theoretical physics*, pp. 420–422. Springer, 1975.
- Levitin, E. S. and Polyak, B. T. Constrained minimization methods. *USSR Computational Mathematics and Mathematical Physics*, 6(5):1–50, 1966.
- Loiseau, J.-C. and Brunton, S. L. Constrained sparse Galerkin regression. *Journal of Fluid Mechanics*, 838: 42–67, 2018.

- Michaelis, L. and Menten, M. L. *Die Kinetik der Invertinwirkung*. Universitätsbibliothek Johann Christian Senckenberg, 2007.
- Morozov, V. On the solution of functional equations by the method of regularization. *Sviet Math. Dokl.*, 7: 414–417, 1966.
- Nesterov, Y. *Lectures on convex optimization*, volume 137. Springer, 2018.
- Nesterov, Y. E. A method for solving the convex programming problem with convergence rate $O(1/k^2)$. In *Dokl. akad. nauk Sssr*, volume 269, pp. 543–547, 1983.
- Noether, E. Invariante Variationsprobleme. Nachrichten der Königlich-Gesellschaft der Wissenschaften. Mathematisch-Physikalische Klasse 2, 235–257. *Transport Theory and Statistical Physics*, pp. 183–207, 1918.
- Rudy, S. H., Brunton, S. L., Proctor, J. L., and Kutz, J. N. Data-driven discovery of partial differential equations. *Science Advances*, 3(4):e1602614, 2017.
- Rudy, S. H., Kutz, J. N., and Brunton, S. L. Deep learning of dynamics and signal-noise decomposition with time-stepping constraints. *Journal of Computational Physics*, 396:483–506, 2019.
- Schaeffer, H. Learning partial differential equations via data discovery and sparse optimization. *Proceedings of the Royal Society A: Mathematical, Physical and Engineering Sciences*, 473(2197):20160446, 2017.
- Schaeffer, H. and McCalla, S. G. Sparse model selection via integral terms. *Physical Review E*, 96(2):023302, 2017.
- Schmidt, M. and Lipson, H. Distilling free-form natural laws from experimental data. *Science*, 324(5923): 81–85, 2009.
- Tibshirani, R. Regression shrinkage and selection via the lasso. *Journal of the Royal Statistical Society: Series B (Methodological)*, 58(1):267–288, 1996.
- Tibshirani, R. J. et al. The lasso problem and uniqueness. *Electronic Journal of statistics*, 7:1456–1490, 2013.
- Wainwright, M. J. Sharp thresholds for high-dimensional and noisy sparsity recovery using ℓ_1 -constrained quadratic programming (lasso). *IEEE transactions on information theory*, 55(5):2183–2202, 2009.
- Zhang, L. and Schaeffer, H. On the convergence of the SINDy algorithm. *Multiscale Modeling & Simulation*, 17(3):948–972, 2019.
- Zheng, P., Askham, T., Brunton, S. L., Kutz, J. N., and Aravkin, A. Y. A unified framework for sparse relaxed regularized regression: Sr3. *IEEE Access*, 7:1404–1423, 2018.

Appendix A. Preliminaries

Given a differentiable function $f(\mathbf{x}) : \mathbb{R}^d \rightarrow \mathbb{R}$ we say the function $f(\mathbf{x})$ is:

Definition A.1 (L -smooth). A function is L -smooth if for any $\mathbf{x}, \mathbf{y} \in \mathbb{R}^d$ we have:

$$f(\mathbf{x}) \leq f(\mathbf{y}) + \langle \nabla f(\mathbf{y}), \mathbf{y} - \mathbf{x} \rangle + \frac{L}{2} \|\mathbf{x} - \mathbf{y}\|^2.$$

This is equivalent to the gradient of $f(\mathbf{x})$ being L -Lipschitz. If the function is twice-differentiable this is equivalent to:

$$0 < L = \max_{\mathbf{x}, \mathbf{y} \in \mathbb{R}^d} \frac{(\mathbf{x} - \mathbf{y})^T \nabla^2 f(\mathbf{x})(\mathbf{x} - \mathbf{y})}{\|\mathbf{x} - \mathbf{y}\|^2} \quad (\text{A.1})$$

Definition A.2 (Convex). A function is convex if for any $\mathbf{x}, \mathbf{y} \in \mathbb{R}^d$ we have:

$$f(\mathbf{x}) \geq f(\mathbf{y}) + \langle \nabla f(\mathbf{y}), \mathbf{y} - \mathbf{x} \rangle$$

If the function is twice-differentiable this is equivalent to:

$$0 = \min_{\mathbf{x}, \mathbf{y} \in \mathbb{R}^d} \frac{(\mathbf{x} - \mathbf{y})^T \nabla^2 f(\mathbf{x})(\mathbf{x} - \mathbf{y})}{\|\mathbf{x} - \mathbf{y}\|^2} \quad (\text{A.2})$$

Definition A.3 (μ -strongly convex). A function is μ -strongly convex if for any $\mathbf{x}, \mathbf{y} \in \mathbb{R}^d$ we have:

$$f(\mathbf{x}) \geq f(\mathbf{y}) + \langle \nabla f(\mathbf{y}), \mathbf{y} - \mathbf{x} \rangle + \frac{\mu}{2} \|\mathbf{x} - \mathbf{y}\|^2.$$

If the function is twice-differentiable this is equivalent to:

$$0 < \mu = \min_{\mathbf{x}, \mathbf{y} \in \mathbb{R}^d} \frac{(\mathbf{x} - \mathbf{y})^T \nabla^2 f(\mathbf{x})(\mathbf{x} - \mathbf{y})}{\|\mathbf{x} - \mathbf{y}\|^2} \quad (\text{A.3})$$

Given a compact convex set $\mathcal{X} \subset \mathbb{R}^d$ we define the constrained optimization problem:

$$\min_{\mathbf{x} \in \mathcal{X}} f(\mathbf{x}). \quad (\text{A.4})$$

Appendix B. Accelerated Projected Gradient Descent

In this section we will focus in the case where $f(\mathbf{x})$ is L -smooth and convex (or potentially μ -strongly convex). One of the key characteristics of convex problems is that any local minima to the problem in Equation (A.4) is a global minima. Moreover, there exist efficient algorithms for computing the minima of these problems. In order to tackle the problem shown in Equation (A.4), one can, for example, use either a projection-based or a projection-free methods, depending on how computationally difficult it is to compute projections onto \mathcal{X} . We denote the *Euclidean projection* of \mathbf{x} onto \mathcal{X} as $\Pi_{\mathcal{X}}(\mathbf{x}) : \mathbb{R}^n \rightarrow \mathcal{X}$, which is defined as:

$$\Pi_{\mathcal{X}}(\mathbf{x}) \stackrel{\text{def}}{=} \operatorname{argmin}_{\mathbf{y} \in \mathcal{X}} \frac{1}{2} \|\mathbf{x} - \mathbf{y}\|^2.$$

In general, computing these projections is non-trivial. However, for a series of structured feasible regions there are closed-form expressions for these projections, which can be computed efficiently (see Table 1):

Feasible region \mathcal{X}	Mathematical expression	Projection
Unit probability simplex	$\{\mathbf{x} \in \mathbb{R}^d \mid \mathbf{1}_d^T \mathbf{x} = 1, \mathbf{x} \geq \mathbf{0}\}$	$\mathcal{O}(d)$
ℓ_p -ball, $p \in \{1, 2, +\infty\}$	$\{\mathbf{x} \in \mathbb{R}^d \mid \ \mathbf{x}\ _p \leq 1\}$	$\mathcal{O}(d)$
Nuclear norm-ball	$\{\mathbf{X} \in \mathbb{R}^{m \times n} \mid \ \mathbf{X}\ _{\text{nuc}} \leq 1\}$	$\mathcal{O}(mn \min\{m, n\})$
Matroid polytope	$\{\mathbf{x} \in \mathbb{R}^d \mid \forall S \in \mathcal{P}(E), \mathbf{1}_S^T \mathbf{x} \leq r(S), \mathbf{x} \geq \mathbf{0}\}$	$\mathcal{O}(\text{poly}(d))$

Table 1: Complexities of projections onto several feasible regions.

Fortunately, projections onto the probability simplex can be computed very efficiently, which makes *accelerated projected descent algorithms* an attractive alternative when solving constrained convex problems over the probability simplex (as is the case in Line 6 of Algorithm 2). These algorithms are termed *accelerated* because they are able to improve upon the convergence guarantees offered by the standard projected gradient descent algorithm, both in the convex case (see Algorithm 4) and in the strongly convex case (see Algorithm 5). If we measure optimality by the number of iterations k needed for the algorithms to achieve an ϵ -optimal accuracy (which means that $f(\mathbf{x}_k) - \min_{\mathbf{x} \in \mathcal{X}} f(\mathbf{x}) \leq \epsilon$), then in the smooth convex case the accelerated projected gradient descent algorithm is able to reach an ϵ -optimal solution in $\mathcal{O}(1/\sqrt{\epsilon})$ iterations, as opposed to the $\mathcal{O}(1/\epsilon)$ iterations needed with standard projected gradient descent. In the smooth and strongly convex case the accelerated projected gradient descent achieves an ϵ -optimal solution in $\mathcal{O}(\sqrt{\mu/L} \log 1/\epsilon)$ iterations, as opposed to the $\mathcal{O}(\mu/L \log 1/\epsilon)$ iterations needed for the standard projected gradient descent algorithm.

Algorithm 4: Accelerated gradient descent for smooth convex problems.

Input : Objective function $f(\mathbf{x})$, feasible region \mathcal{X} , initial point $\mathbf{x}_0 \in \mathcal{X}$.
Output : Point $\mathbf{x}_{K+1} \in \mathcal{X}$.

```

1  $\mathbf{y}_0 \leftarrow \mathbf{x}_0$ 
2  $L \leftarrow \max_{\mathbf{x}, \mathbf{y} \in \mathcal{X}} (\mathbf{x} - \mathbf{y})^T \nabla^2 f(\mathbf{x})(\mathbf{x} - \mathbf{y}) / \|\mathbf{x} - \mathbf{y}\|^2$ 
3  $\gamma_0 \leftarrow 0$ 
4 for  $k = 1$  to  $K$  do
5    $\mathbf{x}_{k+1} \leftarrow \Pi_{\mathcal{X}} \left( \mathbf{y}_k - \frac{1}{L} \nabla f(\mathbf{y}_k) \right)$ 
6    $\gamma_{k+1} \leftarrow \frac{1 + \sqrt{1 + 4\gamma_k^2}}{2}$ 
7    $\mathbf{y}_{k+1} \leftarrow \mathbf{x}_{k+1} + \frac{\gamma_k - 1}{\gamma_{k+1}} (\mathbf{x}_{k+1} - \mathbf{x}_k)$ 
8 end

```

Algorithm 5: Accelerated gradient descent for smooth strongly-convex problems.

Input : Objective function $f(\mathbf{x})$, feasible region \mathcal{X} , initial point $\mathbf{x}_0 \in \mathcal{X}$.
Output : Point $\mathbf{x}_{K+1} \in \mathcal{X}$.

```

1  $\mathbf{y}_0 \leftarrow \mathbf{x}_0$ 
2  $\mu \leftarrow \min_{\mathbf{x}, \mathbf{y} \in \mathcal{X}} (\mathbf{x} - \mathbf{y})^T \nabla^2 f(\mathbf{x})(\mathbf{x} - \mathbf{y}) / \|\mathbf{x} - \mathbf{y}\|^2$ 
3  $L \leftarrow \max_{\mathbf{x}, \mathbf{y} \in \mathcal{X}} (\mathbf{x} - \mathbf{y})^T \nabla^2 f(\mathbf{x})(\mathbf{x} - \mathbf{y}) / \|\mathbf{x} - \mathbf{y}\|^2$ 
4 for  $k = 1$  to  $K$  do
5    $\mathbf{x}_{k+1} \leftarrow \Pi_{\mathcal{X}} \left( \mathbf{y}_k - \frac{1}{L} \nabla f(\mathbf{y}_k) \right)$ 
6    $\mathbf{y}_{k+1} \leftarrow \mathbf{x}_{k+1} + \frac{1 - \sqrt{\mu/L}}{1 + \sqrt{\mu/L}} (\mathbf{x}_{k+1} - \mathbf{x}_k)$ 
7 end

```

Appendix C. On computing integrals and derivatives from noisy data

One of the key requirements for the success of any sparse recovery algorithm is the accurate estimation of integrals and derivatives. We are typically given a dictionary of basis functions $\mathcal{D} = \{\psi_i \mid i \in \llbracket 1, n \rrbracket\}$ that can be used to represent our dynamic, encoded by $\dot{\mathbf{x}}(t) = \Xi^T \psi(\mathbf{x}(t))$, where $\Xi \in \mathbb{R}^{n \times d}$ and $\psi(\mathbf{x}(t)) = [\psi_1(\mathbf{x}(t)), \dots, \psi_n(\mathbf{x}(t))]^T \in \mathbb{R}^n$ along with some data points. Ideally, we would like to observe a series of noise-free data points from the physical system $\{\mathbf{x}(t_i)\}_{i=1}^m$. We would also like to observe $\{\dot{\mathbf{x}}(t_i)\}_{i=1}^m$, if we follow the differential approach, so that we can construct the matrix \dot{X} in the left-hand side of Equation (C.1). Or we would like to observe $\{\int_{t_1}^{t_i+1} \psi_i(\mathbf{x}(\tau)) d\tau\}_{i=1}^{m-1}$ for all $i \in \llbracket 1, n \rrbracket$, if we follow the integral approach, so that we can construct the $\Gamma(X)$ matrix on the right-hand side of Equation (C.1).

Noise-free LASSO Differential approach	Noise-free LASSO Integral approach
$\operatorname{argmin}_{\substack{\ \Omega\ _{1,1} \leq \alpha \\ \Omega \in \mathbb{R}^{n \times d}}} \ \dot{X} - \Omega^T \Psi(X)\ _F^2$	$\operatorname{argmin}_{\substack{\ \Omega\ _{1,1} \leq \alpha \\ \Omega \in \mathbb{R}^{n \times d}}} \ \delta X - \Omega^T \Gamma(X)\ _F^2 \quad (\text{C.1})$

However, in general we do not observe either of these quantities, and have to estimate \dot{X} and $\Gamma(X)$ from $\{\mathbf{x}(t_i)\}_{i=1}^m$. The estimation of these matrices is made even more difficult if we are only able to observe noise-corrupted data points $\{\mathbf{y}(t_i)\}_{i=1}^m$ such that $\mathbf{y}(t_i) = \mathbf{x}(t_i) + \mathbf{v}(t_i)$, where $\{\mathbf{v}(t_i)\}_{i=1}^m$ is a set of i.i.d. noise vectors, which is typically the case. In this case, we can only work with a noisy matrix Y , with which we either have to estimate $\dot{Y} \in \mathbb{R}^{d \times m}$ or $\Gamma(Y) \in \mathbb{R}^{n \times m-1}$. The error in the formulation now comes from both the noisy data, and from the estimation of the derivatives/integrals from noisy data. The question then becomes, how do $\|\dot{Y} - \dot{X}\|_F$ and $\|\Gamma(Y) - \Gamma(X)\|_F$ evolve as we increase the noise? Given data contaminated with noise, is it easier to get an accurate estimate of \dot{Y} than of $\Gamma(Y)$? If so, we might favor one approach over the other.

For example if we let the Fermi-Pasta-Ulam-Tsingou system with $d = 5$ evolve from a random initial state, and we sample the system T/c times at regularly spaced intervals, and we repeat this experiment $c = 60$ times, we generate $T = 2400$ data points $\mathbf{x}^j(t_i)$ with $i \in \llbracket 1, T/c \rrbracket$ and $j \in \llbracket 1, c \rrbracket$, with $t_{T/c} = 3$ seconds. We can proceed to corrupt these data points with Gaussian noise as in Section 4, generating data points with $\mathbf{y}^j(t_i) = \mathbf{x}^j(t_i) + \alpha \mathcal{N}(0, \Sigma)$. In this case we need to estimate \dot{X} if we want to formulate the problem from a differential perspective, or \dot{X} if we want to formulate the problem from an integral perspective. Using the same dictionary of basis functions as the ones used in Section 4.3, we use the first-order central difference rule as well as differentiation of local polynomial interpolations to estimate the first derivative of X with respect to time, using Y . The results are shown on the image of the left in Figure 11. We also use the second-order central difference formula, as well as differentiation of local polynomial interpolations to estimate the second derivative of X with respect to time, using Y . The results can be seen on the image to the right in Figure 11.

We also use Simpsons quadrature rules as well as integration of local polynomial interpolations to estimate the integral $\Gamma(\dot{X})$ using \dot{Y} , which is our estimate of \dot{X} , the errors when computing these integrals with the aforementioned methods are shown in Figure 12.

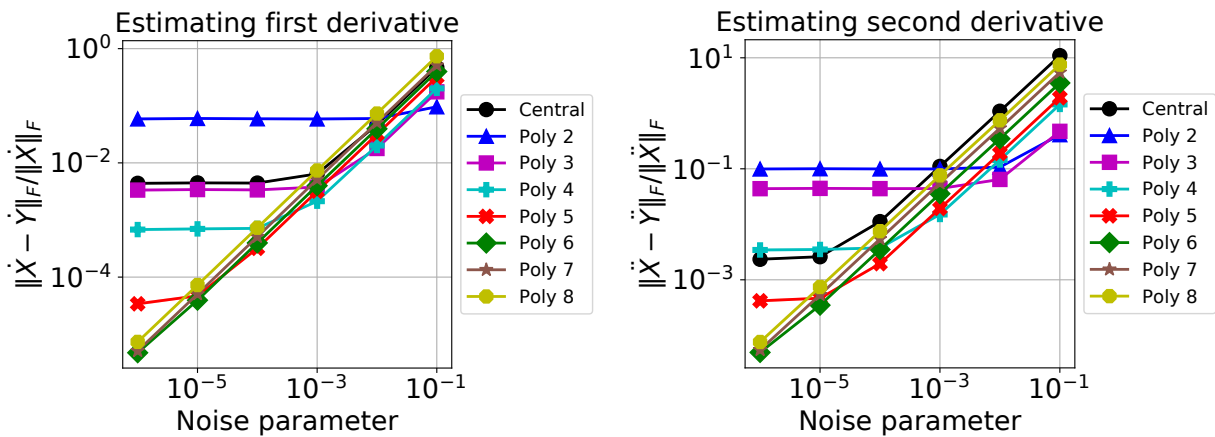


Figure 11: **Fermi-Pasta-Ulam-Tsingou:** Comparison of estimates of first and second derivatives with respect to time with exact first and second order derivatives.

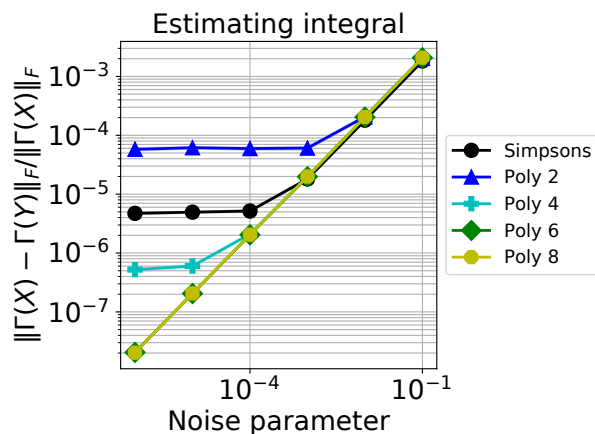


Figure 12: **Fermi-Pasta-Ulam-Tsingou:** Comparison of estimates of first and second derivatives with respect to time with exact first and second order derivatives.

Regarding the errors shown between approximating \dot{X} and \ddot{X} , for a given method we expect the errors estimating \ddot{X} to be higher than the ones in estimating \dot{X} , which is what we observe in the experiments. There is no direct way to make a fair comparison between an approximation to the matrices \dot{X} and \ddot{X} and an approximation to the matrix $\Gamma(\dot{X})$, given their different nature (and even size), however if we use the metric $\|\dot{X} - \dot{Y}\|_F / \|\dot{X}\|_F$, $\|\ddot{X} - \ddot{Y}\|_F / \|\ddot{X}\|_F$ and $\|\Gamma(\dot{X}) - \Gamma(\dot{Y})\|_F / \|\Gamma(\dot{X})\|_F$ to compare the two approximations, the data seems to suggest that it is easier to estimate the matrix $\Gamma(\dot{X})$ than it is to estimate \ddot{X} , at least in the current experiment with the Fermi-Pasta-Ulam-Tsingou model.

Appendix D. Additional figures

The images shown in Figure 13 and 14 show the objective function evaluation for the constrained version of the Kuramoto LASSO problem with $d = 5$ and $d = 10$, respectively. The objective function is evaluated for the different methods, for both the training data and the testing data and the differential and integral formulation.

The images shown in Figure 15 and 16 show the objective function evaluation for the constrained version of the Fermi-Pasta-Ulam-Tsingou LASSO problem with $d = 5$ and $d = 10$, respectively. The objective function is evaluated for the different methods, for both the training data and the testing data and the differential and integral formulation.

The images shown in Figure 17 show the objective function evaluation for the constrained version of the Michaelis-Menten LASSO problem with $d = 4$. The objective function is evaluated for the different methods, for both the training data and the testing data and the differential and integral formulation.

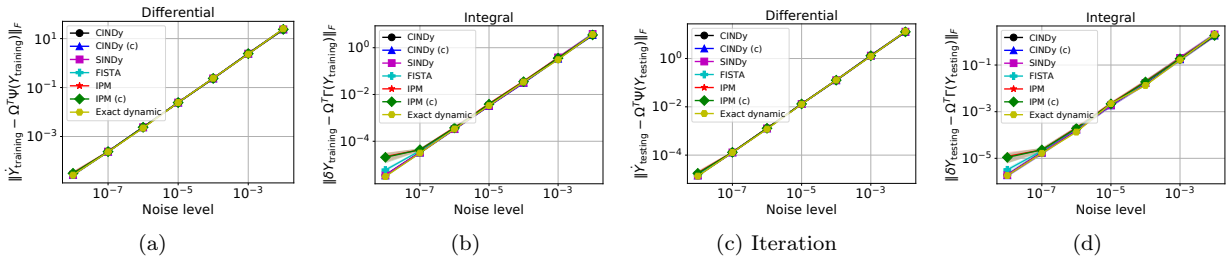


Figure 13: Kuramoto: Evaluation of $\|\dot{Y}_{\text{training}} - \Omega^T \Psi(Y_{\text{training}})\|_F$ (a) for the differential formulation, and $\|\delta \dot{Y}_{\text{training}} - \Omega^T \Gamma(Y_{\text{training}})\|_F$ (b) for the integral formulation for the experiments with $d = 5$, and evaluation of $\|\dot{Y}_{\text{validation}} - \Omega^T \Psi(Y_{\text{validation}})\|_F$ (c) for the differential formulation, and $\|\delta \dot{Y}_{\text{validation}} - \Omega^T \Gamma(Y_{\text{validation}})\|_F$ (d) for the integral formulation for the experiments with $d = 5$.

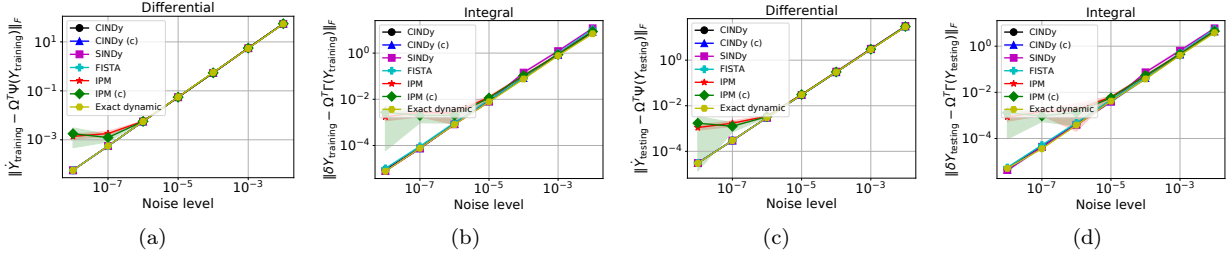


Figure 14: Kuramoto: Evaluation of $\|\dot{Y}_{\text{training}} - \Omega^T \Psi(Y_{\text{training}})\|_F$ (a) for the differential formulation, and $\|\delta \dot{Y}_{\text{training}} - \Omega^T \Gamma(Y_{\text{training}})\|_F$ (b) for the integral formulation for the experiments with $d = 10$, and evaluation of $\|\dot{Y}_{\text{validation}} - \Omega^T \Psi(Y_{\text{validation}})\|_F$ (c) for the differential formulation, and $\|\delta \dot{Y}_{\text{validation}} - \Omega^T \Gamma(Y_{\text{validation}})\|_F$ (d) for the integral formulation for the experiments with $d = 10$.

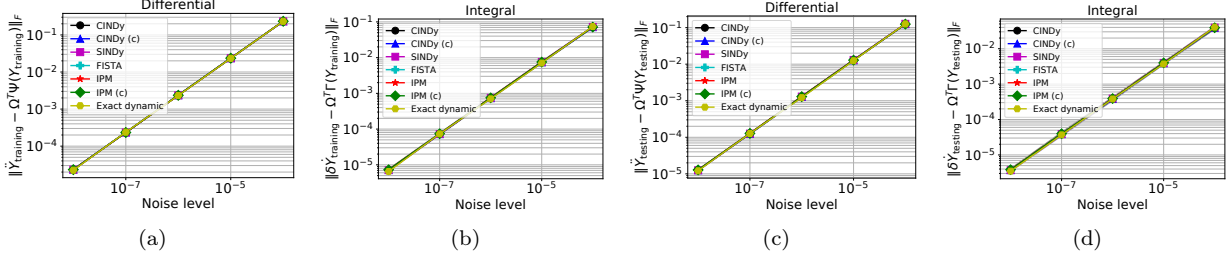


Figure 15: Fermi-Pasta-Ulam-Tsingou: Evaluation of $\|\dot{Y}_{\text{training}} - \Omega^T \Psi(Y_{\text{training}})\|_F$ (a) for the differential formulation and $\|\delta \dot{Y}_{\text{training}} - \Omega^T \Gamma(Y_{\text{training}})\|_F$ (b) for the integral formulation with $d = 5$, and evaluation of $\|\dot{Y}_{\text{validation}} - \Omega^T \Psi(Y_{\text{validation}})\|_F$ (c) for the differential formulation, and $\|\delta \dot{Y}_{\text{validation}} - \Omega^T \Gamma(Y_{\text{validation}})\|_F$ (d) for the integral formulation with $d = 5$.

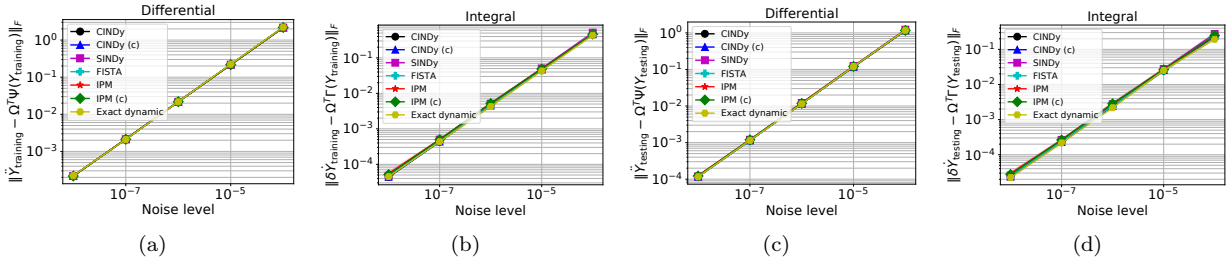


Figure 16: Fermi-Pasta-Ulam-Tsingou: Evaluation of $\|\dot{Y}_{\text{training}} - \Omega^T \Psi(Y_{\text{training}})\|_F$ (a) for the differential formulation and $\|\delta \dot{Y}_{\text{training}} - \Omega^T \Gamma(Y_{\text{training}})\|_F$ (b) for the integral formulation with $d = 10$, and evaluation of $\|\dot{Y}_{\text{validation}} - \Omega^T \Psi(Y_{\text{validation}})\|_F$ (c) for the differential formulation, and $\|\delta \dot{Y}_{\text{validation}} - \Omega^T \Gamma(Y_{\text{validation}})\|_F$ (d) for the integral formulation with $d = 10$.

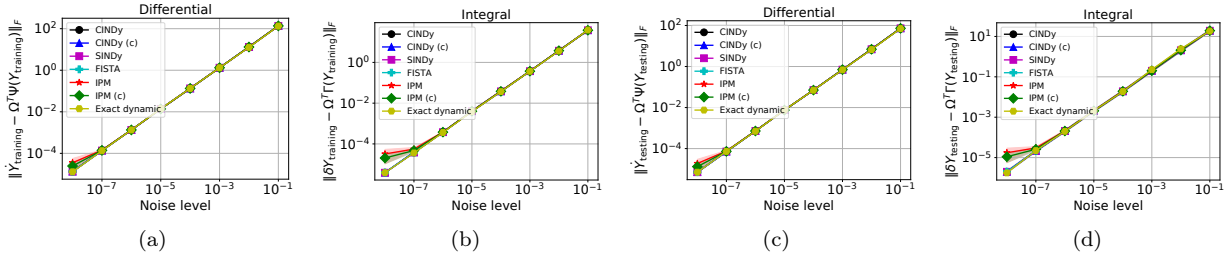


Figure 17: Michaelis-Menten: Evaluation of $\|\dot{Y}_{\text{training}} - \Omega^T \Psi(Y_{\text{training}})\|_F$ (a) for the differential formulation, and $\|\delta \dot{Y}_{\text{training}} - \Omega^T \Gamma(Y_{\text{training}})\|_F$ (b) for the integral formulation with $d = 4$, and evaluation of $\|\dot{Y}_{\text{validation}} - \Omega^T \Psi(Y_{\text{validation}})\|_F$ (c) for the differential formulation, and $\|\delta \dot{Y}_{\text{validation}} - \Omega^T \Gamma(Y_{\text{validation}})\|_F$ (d) for the integral formulation with $d = 4$.

Appendix E. Sample efficiency

The images shown in Figure 18, 19, and 20 show the evolution of \mathcal{E}_R , \mathcal{S}_E and \mathcal{S}_M as we vary the number of training data points when learning the Kuramoto dynamic ($d = 5$) with the dictionary described in Section 4.2. The images show the resulting metrics when generating 50 data points per experiment and using local polynomial interpolation of degree 8 to compute the derivatives and the integrals.

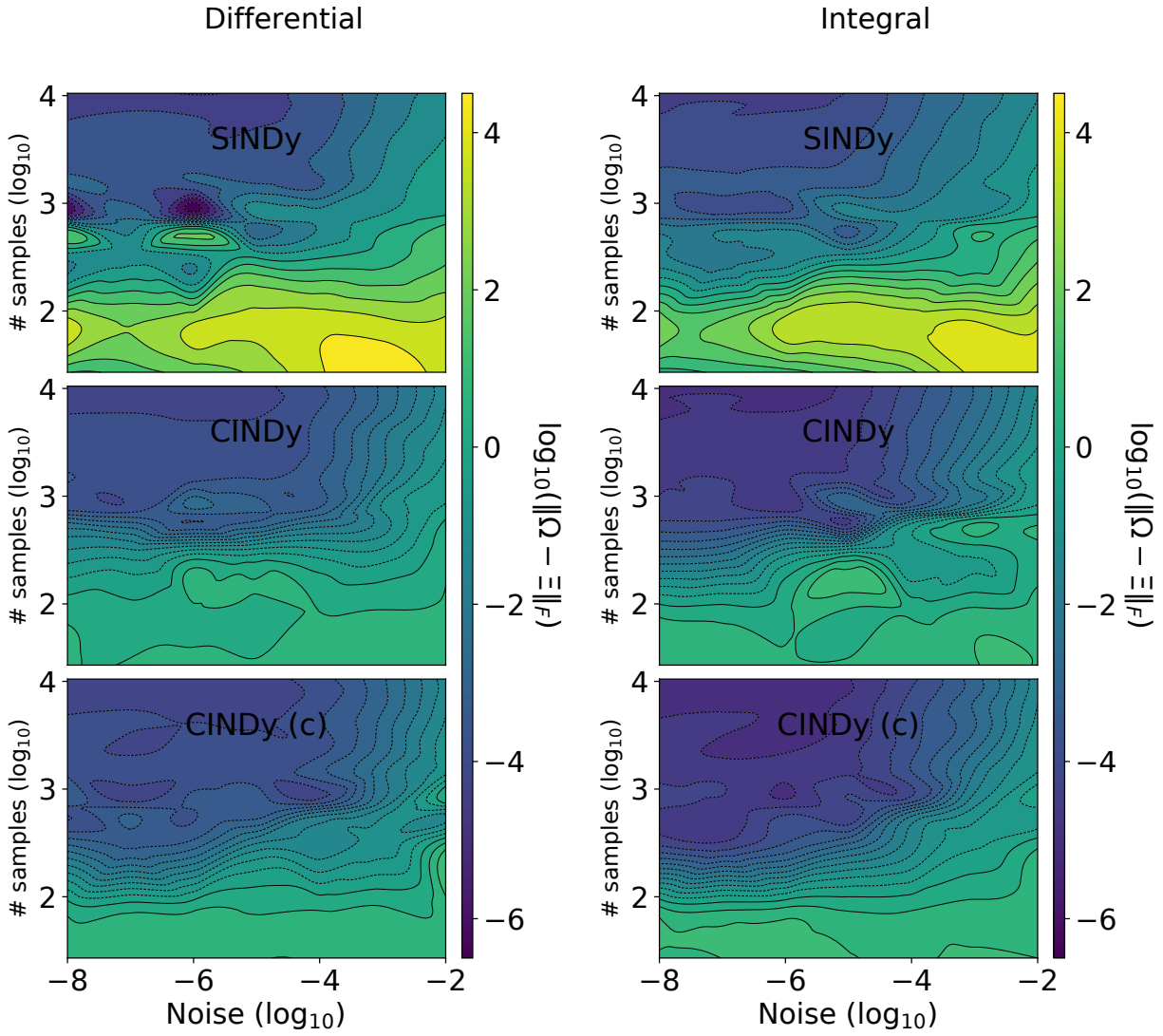


Figure 18: **Sample efficiency of the sparse recovery of the Kuramoto model:** Algorithm comparison in terms of \mathcal{E}_R for a Kuramoto model of dimension $d = 5$ for the differential formulation (left) and the integral formulation (right).

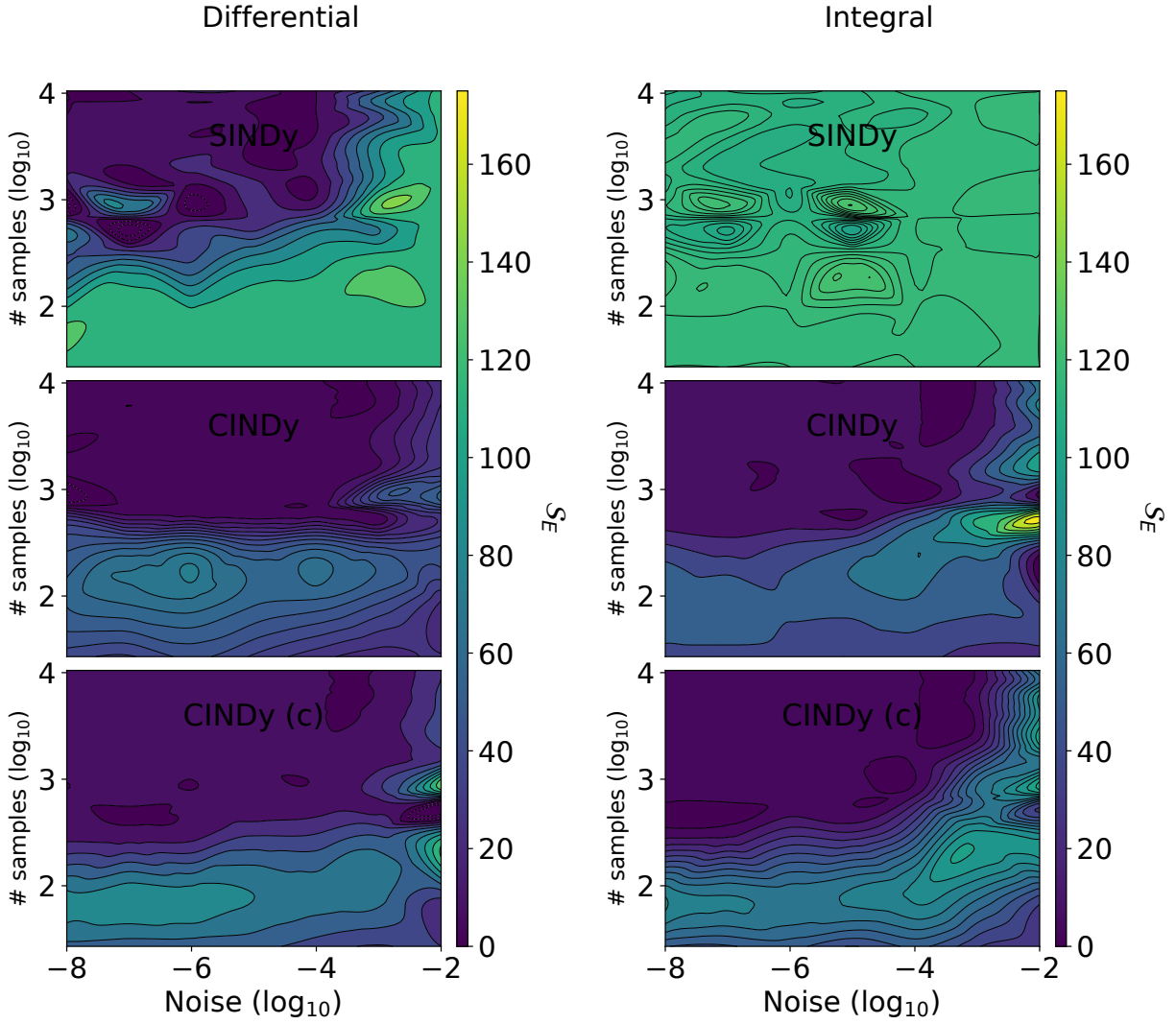


Figure 19: **Sample efficiency of the sparse recovery of the Kuramoto model:** Algorithm comparison in terms of S_E for a Kuramoto model of dimension $d = 5$ for the differential formulation (left) and the integral formulation (right).

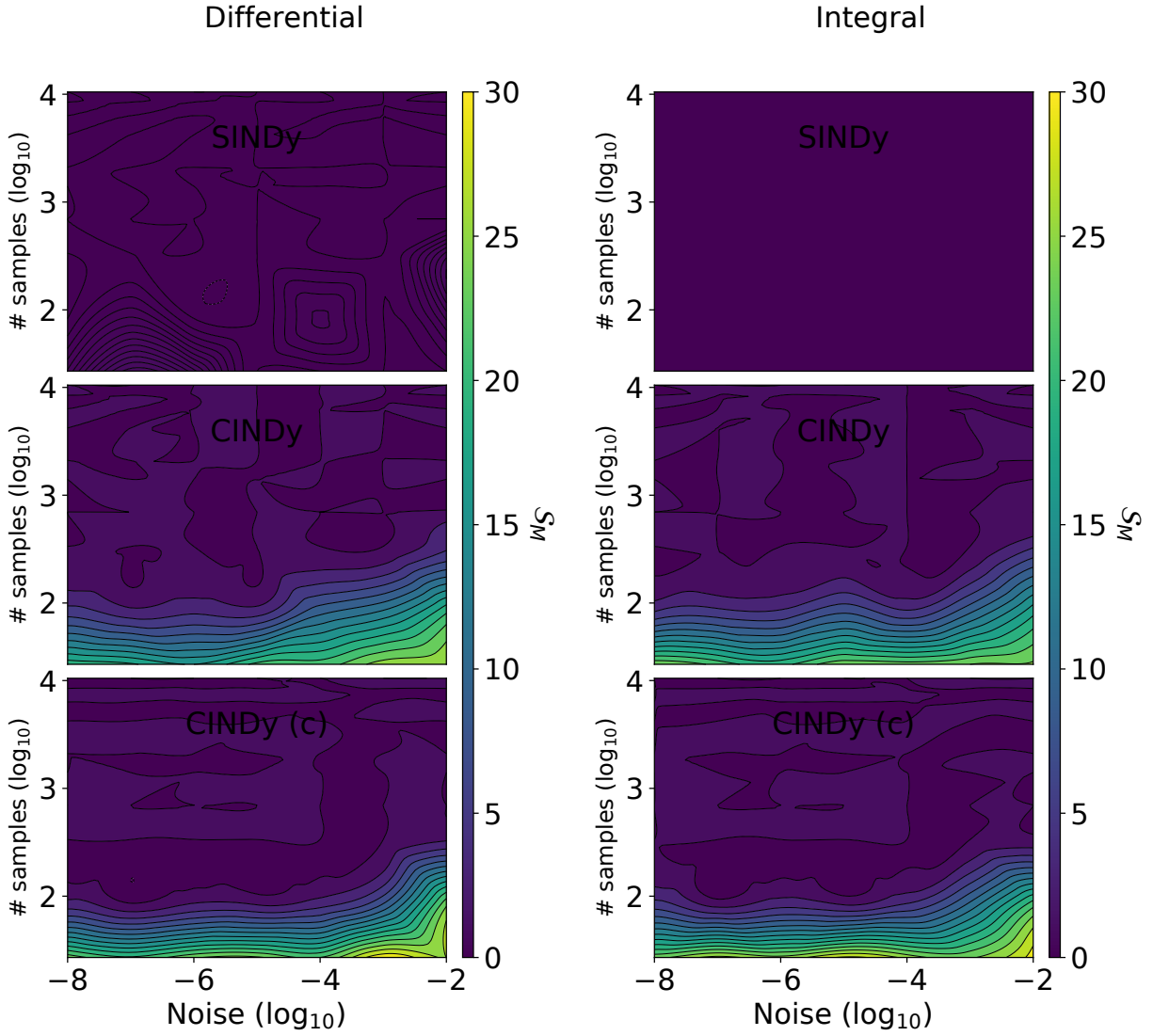


Figure 20: **Sample efficiency of the sparse recovery of the Kuramoto model:** Algorithm comparison in terms of S_M for a Kuramoto model of dimension $d = 5$ for the differential formulation (left) and the integral formulation (right).